

AD-A154 073

DEFORMATION FRACTURE AND EXPLOSIVE PROPERTIES OF
REACTIVE MATERIALS(U) CAMBRIDGE UNIV (ENGLAND)
CAVENDISH LAB J E FIELD ET AL FEB 85 R/D-4380-R-AN

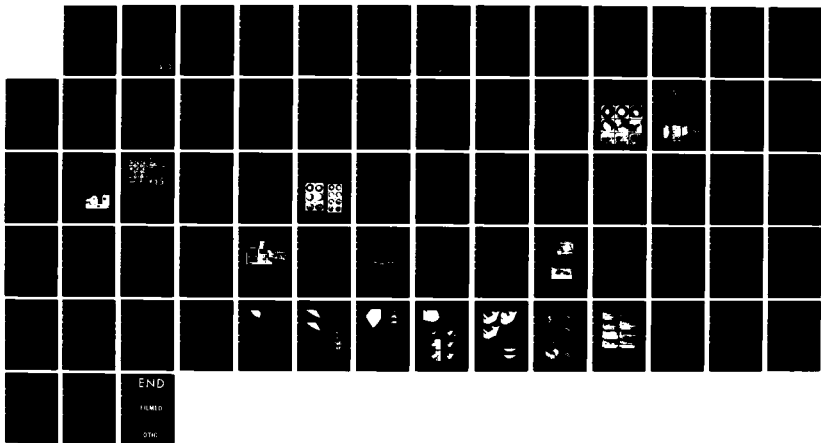
1/1

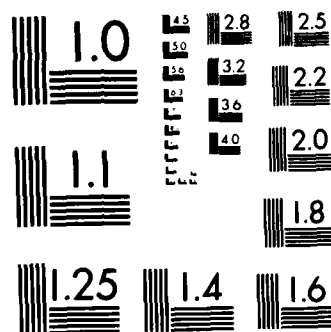
UNCLASSIFIED

DAJA45-84-C-0018

F/G 19/1

NL





MICROCOPY RESOLUTION TEST CHART
NATIONAL BUREAU OF STANDARDS 1963-A

AD-A154 073

4380-R-AN

AD

(2)

DEFORMATION, FRACTURE AND EXPLOSIVE PROPERTIES
OF REACTIVE MATERIALS

Annual Report

by

Dr. J.E. Field, Dr. M.M. Chaudhri, Dr. K. Mohan,
Dr. G.M. Swallowe and Dr. W.L. Ng

FEBRUARY 1985

EUROPEAN RESEARCH OFFICE

United States Army
London W1, England

Contract Number DAJA45-84-C-0018

Physics and Chemistry of Solids
Cavendish Laboratory
Madingley Road
Cambridge CB3 OHE, UK

Approved for public release; distribution unlimited

DTIC FILE COPY

DTIC
ELECTE
S D
MAY 23 1985
B

85 4 19 012
85 4 19 012

REPORT DOCUMENTATION PAGE		READ INSTRUCTIONS BEFORE COMPLETING FORM
1. REPORT NUMBER	2. GOVT ACCESSION NO.	3. RECIPIENT'S CATALOG NUMBER
4. TITLE (and Subtitle) DEFORMATION, FRACTURE AND EXPLOSIVE PROPERTIES OF REACTIVE MATERIALS.		5. TYPE OF REPORT & PERIOD COVERED ANNUAL JAN 1984 to DEC 1984
7. AUTHOR(s) Dr. J.E. Field, Dr. M.M. Chaudhri, Dr. K. Mohan, Dr. G.M. Swallowe, Dr. W.L. Ng		6. PERFORMING ORG. REPORT NUMBER DAJA45-84-C-0018
9. PERFORMING ORGANIZATION NAME AND ADDRESS Physics & Chemistry of Solids Group, Cavendish Laboratory, Madingley Road, Cambridge CB3 OHE, U.K.		10. PROGRAM ELEMENT, PROJECT, TASK AREA & WORK UNIT NUMBERS
11. CONTROLLING OFFICE NAME AND ADDRESS		12. REPORT DATE FEBRUARY 1985
		13. NUMBER OF PAGES 67
14. MONITORING AGENCY NAME & ADDRESS(if different from Controlling Office)		15. SECURITY CLASS. (of this report)
		15a. DECLASSIFICATION/DOWNGRADING SCHEDULE
16. DISTRIBUTION STATEMENT (of this Report) APPROVED FOR PUBLIC RELEASE: DISTRIBUTION UNLIMITED.		
17. DISTRIBUTION STATEMENT (of the abstract entered in Block 20, if different from Report)		
18. SUPPLEMENTARY NOTES		
19. KEY WORDS (Continue on reverse side if necessary and identify by block number) EXPLOSIVES, IGNITION, IMPACT, SENSITIVENESS, HOT SPOTS, DECOMPOSITION, KINETICS, DEFORMATION, FRACTURE, PBX's, HMX, HNS, PETN.		
20. ABSTRACT (Continue on reverse side if necessary and identify by block number) The report covers four areas of work. The first describes a study of the initiation of HNS under drop-weight impact using high-speed photography. Ignition is shown to take place after rapid mechanical deformation of the sample. The behaviour is compared to that of a range of other explosives. From a comparison of the melting points, yield stresses, flow properties and ignition characteristics it appears that explosives with high strength values are more likely to exhibit rapid mechanical failure and resultant ignition.		

during impact. The report then describes the range of techniques which we have developed for studies of the deformation, strength and ignition properties of explosives. They include an instrumented drop-weight test, a novel drop-weight apparatus with transparent anvils which allows high-speed photographic observation of the impact and ignition processes. Laser-speckle, used in conjunction with a specimen loaded in the Brazilian test geometry which gives tensile strengths and strain to failures of PBX's and a modified Hopkinson bar apparatus which gives data on explosives up to strain rates of 5×10^4 s⁻¹. The next section describes the results of a detailed study of the decomposition of PETN using time-of-flight mass spectrometry. The decomposition was induced by heating slowly, by fracturing single crystals and by laser irradiation. Different reaction pathways were found in each case and these are discussed. Finally, an experimental study is described in which the deformation stress of millimeter-size single crystals of explosive materials has been determined using a novel experimental technique. The method involved the loading of the test crystal against a transparent glass plate with in situ measurements of the real area of contact under load using an optical microscope. For all explosive crystals the deformation stress was found to increase with load reaching a plateau at higher loads. The maximum deformation stress of a crystal was found to be considerably lower than its Vickers diamond hardness value.

Indicator Supplied Keywords include
C (U) K (P)

**DEFORMATION, FRACTURE AND EXPLOSIVE PROPERTIES
OF REACTIVE MATERIALS**

<u>TABLE OF CONTENTS</u>	<u>PAGE</u>
1. INTRODUCTION	
1.1 Drop-weight impact studies	1
1.2 High-strain rate properties of explosives	1
1.3 Thermal, fracture and laser-induced decomposition of PETN	2
1.4 The deformation stress of highly brittle explosive crystals from real contact area measurements	2
2. IMPACT INITIATION OF HEXANITROSTILBENE	
ABSTRACT	3
1. Introduction	4
2. Experimental	5
3. Results & Discussions:	
Photographic observation of the impact	6
Impact behaviour in the drop-weight test	8
Strength and sensitivity relation	10
ACKNOWLEDGEMENTS	12
REFERENCES	13
TABLE 1	14
TABLE 2	15
FIGURE LEGENDS	16
3. HIGH STRAIN RATE PROPERTIES OF EXPLOSIVES	
ABSTRACT	17
1. Introduction	17
2. Experimental	18
3. Results:	
3.1 Pure Explosive	19
3.2 Explosives with Polymer Additives	21
3.3 PBX's	22
CONCLUSION	24
ACKNOWLEDGEMENTS	24
REFERENCES	24

4. THERMAL, FRACTURE AND LASER-INDUCED DECOMPOSITION**OF PETN**

ABSTRACT	25
1. Introduction	26
2. Thermal decomposition	27
3. Experimental	28
a) Fracture-Induced Decomposition	29
i) Less energetic fracture	29
ii) Energetic fracture	29
b) Laser-Induced Decomposition	30
c) Laser Initiation	30
4. Results:	
a) Fracture-Induced Decomposition	30
b) Laser-Induced Decomposition	31
c) Laser Initiation	32
5. Discussion:	
a) Fracture-Induced Decomposition	33
b) Laser-Induced Decomposition	37
c) Laser Ignition of PETN	41
CONCLUSION	41
ACKNOWLEDGEMENTS	42
REFERENCES	43
FIGURE CAPTIONS	45

5. THE DEFORMATION STRESS OF HIGHLY BRITTLE EXPLOSIVE**CRYSTALS FROM REAL CONTACT AREA MEASUREMENTS**

ABSTRACT	46
1. Introduction	46
2. Experimental details:	
2.1 Materials	46
2.2 The principle of the experimental technique	47
2.3 The compression apparatus	47
3. Results:	
3.1 α -PbN ₆	48
3.2 LAT	50
3.3 β -HMX	51
3.4 RDX	53
3.5 KCl	55
4. Data reduction	56

5. Discussion	57
5.1 Plastic flow at very low loads	57
5.2 The increase of the deformation stress with load	58
5.3 The maximum deformation stress of a crystal against its Vickers diamond hardness	58
5.4 The layer left on the glass plate	58
5.5 Flow stress determination	59
CONCLUSIONS	59
ACKNOWLEDGEMENTS	59
REFERENCES	59

**S DTIC
ELECTE
MAY 23 1985 D**

B



Accession For	<input checked="" type="checkbox"/>
NTIS	<input type="checkbox"/>
Other	<input type="checkbox"/>
Classification	<input type="checkbox"/>
Date	<input type="checkbox"/>
Author	<input type="checkbox"/>
Subject	<input type="checkbox"/>
Source	<input type="checkbox"/>
Language	<input type="checkbox"/>
Format	<input type="checkbox"/>
Series	<input type="checkbox"/>
Notes	<input type="checkbox"/>
Priority Codes	<input type="checkbox"/>
Serial	<input type="checkbox"/>
Special	<input type="checkbox"/>
A-1	

DEFORMATION, FRACTURE AND EXPLOSIVE PROPERTIES
OF REACTIVE MATERIALS

1. INTRODUCTION

In this annual report, we describe four areas of work completed during the grant period. This research has recently been prepared for publication and the full texts of the papers are given.

1.1 Drop-weight impact studies

These have been made using the facilities developed in early work and described by Heavens and Field (1974). Figure 1, of the first paper, illustrates our transparent anvil drop-weight apparatus which allows us to photograph events at microsecond framing rates. Figure 2 is an instrumented drop-weight machine which allows us to record pressure-time curves.

In the grant period, we have made a detailed study of hexanitrostilbene (HNS) and have compared its behaviour with a range of other explosives. The photographic sequences show that upon impact the layer of explosive undergoes bulk plastic flow at speeds of over 250 m s^{-1} . Initiation occurs after this catastrophic failure. From a comparison of melting points, uniaxial yield stress values, flow properties and the ignition characteristics of several organic secondary explosives, it appears that explosives with high strength values are more likely to exhibit both a rapid mechanical failure and resultant ignition during impact. The results emphasize the important relation between mechanical properties and ignition characteristics.

1.2 High strain rate properties of explosives

This second paper was presented at the Second International Conference

on "The Mechanical Properties of Materials at High Rates of Strain", held at Oxford, U.K. in April 1984. The paper describes our experimental facilities which include: (a) drop-weight machines; (b) a technique which uses the so-called "Brazilian" test geometry and laser speckle photography for measurements of the tensile strengths and rupture strains of PBX explosives; and (c) a miniaturised and modified Hopkinson bar apparatus which allows us to record the stress strain curves of explosives at strain rates up to 10^5 s^{-1} . Results are given in this paper for various A.W.R.E. Aldermaston PBX compositions. Recently we have started research on U.S. compositions supplied by Los Alamos.

1.3 Thermal, fracture and laser-induced decomposition of PETN

This project which involved a detailed mass spectrometry study was started a few years ago, but has recently been completed and prepared for publication. It describes the different reaction pathways following slow heating, fracture and laser-irradiation of PETN.

1.4 The deformation stress of highly brittle explosive crystals from real contact area measurements

An experimental study is described in which the deformation stress of mm. size highly brittle as-grown single crystals of explosive materials has been determined using a novel experimental technique. The technique involved the loading of the test crystal against a transparent glass plate with in situ measurements of the real area of contact under load using an optical microscope. For all explosive crystals the deformation stress was found to increase with load reaching a plateau at higher loads. The maximum deformation stress of a crystal was found to be considerably lower than its Vickers diamond hardness value. A discussion on the determination of the uni-axial yield stress of small particles is given.

2. IMPACT INITIATION OF HEXANITROSTILBENE

V. Krishna Mohan and J.E. Field

ABSTRACT

A study has been made of the initiation of hexanitrostilbene (HNS) under impact using high-speed photography at microsecond framing rates. The photographic sequences show that upon impact the layer of explosive undergoes bulk plastic flow at speeds of over 250 m s^{-1} . Initiation occurs after this catastrophic failure of the explosive due to the fact that the adiabatic heating produced by plastic deformation is extremely localized in nature. From a comparison of the melting points, uniaxial yield stress values, flow properties and the ignition characteristics for several organic secondary explosives, it appears that explosives with high strength values are more likely to exhibit both a rapid mechanical failure and resultant ignition during impact. Addition of polycarbonate (PC) has been found to sensitize the explosive. Strain-gauge measurements of impact of pure HNS and HNS/PC samples have shown that a sudden pressure drop occurs before ignition due to rapid failure of the test material, the latter being in agreement with the photographic observations.

I. INTRODUCTION

Hexanitrostilbene (HNS) is a secondary explosive which is used in many applications because of its relative stability at elevated temperatures. Of major concern to explosive formulators is the possibility of accidental initiation during manufacture, transport or usage. One of the standard methods adopted to assess the hazards associated with an explosive is the fall-hammer test in which a sample (typically 20 - 50 mg) is subjected to impact with a falling weight. Repeated series of these tests give some idea about the impact energy necessary to ignite the sample. The results of these tests are usually expressed in terms of H_{50} , where H_{50} refers to the height from which the weight would ignite 50% of a series of samples. Although the test has been used for many decades, it is only recently that a systematic attempt has been made to photograph the sample during its deformation [1-3]. A combination of high-speed photographic and pressure-measuring techniques helped establish the physical processes occurring during ignition and propagation.

The high-speed photographic studies pioneered by Heavens and Field [1] have been useful in identifying the various mechanisms responsible for the formation of initiation sites. In general it is thought that the initiation of explosion by mechanical shock is thermal in origin. On the basis of localized thermal energy or 'hot-spots' as the source of explosion, four possible mechanisms for ignition by impact can be envisaged:

- (i) adiabatic compression of trapped gas spaces [4,5]
- (ii) viscous heating of material rapidly extruded between the impacting surfaces or grains [6,7]
- (iii) friction between the impacting surfaces, the explosive crystals and/or grit particles in the explosive layer [8,9]
- (iv) localized adiabatic shear of the material during mechanical failure [3, 10 - 12]

The references cited above for the various initiation mechanisms are not

exhaustive; a complete list is given in reference 3. Field et al [3] have shown that no one mechanism is the dominant means of ignition and that only very slight changes in the conditions of an experiment can lead to 'hot-spots' being formed by different processes.

The high-speed camera work of Heavens and Field [1] revealed that various phenomena may be involved when a thin layer of material is impacted, including plastic flow, jetting, shear banding and even melting. Ignition occurred at a few 'hot-spots' following severe deformation of the sample. Strain-gauge measurements showed that if a sample failed by plastic flow, a sharp pressure drop occurred of a few hundred MPa. It was after the pressure drop that ignition took place. Of the several explosives examined by these authors, only pentaerythritol tetranitrate (PETN), cyclotrimethylene trinitramine (RDX) and cyclotetramethylene tetranitramine (HMX) exhibited such large pressure drops and ignited after the pressure drop while other explosives such as tetryl and picric acid gave rise to a series of pressure fluctuations to which ignition was not linked. Recent photographic studies on the impact ignition of tetryl indicated that it has comparatively little tendency to flow under impact; the explosion was quite localized at the various ignition sites close to the periphery of the sample and did not propagate into the bulk of the sample [13].

It is clear from the above discussion that there are differences in the mode of ignition for different explosives and it is, therefore, worthwhile to widen the data base by examination of further explosive materials. With this objective in view, the impact behaviour of HNS is investigated in the present work using both photographic and pressure-measuring techniques.

2. EXPERIMENTAL

High-speed photographic observation of the behaviour of a thin layer of explosive was carried out using toughened glass anvils, allowing the impact process to be viewed in transmitted light. An A.W.R.E. designed C4 rotating-mirror camera at framing intervals of ca. 7.0 μ s was used to

photograph the event. Figure 1 shows the experimental arrangement of the impact set-up; details of the apparatus are given in reference 1. In this work, all experiments were made on 25 mg of HNS in crystalline form (particle size 50 - 150 μm), which was impacted by a 5.5 kg weight falling from a height of 1 m. A few trials were carried out by adding polycarbonate (PC) to the explosive.

Experiments were also performed on an instrumented drop-weight machine similar to that described by Heavens and Field [1] (see Figure 2). The apparatus was connected to a self contained data recording system. This comprised a Data Laboratories D1922 transient recorder, a Tektronix double-beam oscilloscope, and a paper tape punch. With this system, analogue signals from the drop-weight apparatus are digitised in real time and retained in memory so that the signals may be subsequently photographed on the oscilloscope and transferred to the paper tape for data analysis. The data was analysed on a HP9825 calculator by using a program based on the method of analysis outlined in references 1 and 10.

3. RESULTS AND DISCUSSION

Photographic observation of the impact.

A sequence illustrating the behaviour of HNS under impact is given in Fig. 3. Frame (a) corresponds to the initial instant of impact while frames (b) and (c) represent the sample after 315 and 434 μs respectively. During the early stages the thin explosive layer is compacted into the form of a pellet. By frame (d) the layer starts to deform plastically and from this stage onwards the flow of material is extremely rapid, attaining speeds of over 250 m s^{-1} . It appears that the explosive, initially opaque, becomes translucent as it undergoes severe plastic deformation presumably due to fusion of particles under impact pressure. Ignition occurs after ca. $450 \mu\text{s}$ at the periphery of the expanding layer and subsequently propagates into the bulk of the sample. The later frames, (f) to (i) show that the central portion which is translucent in frame (e) gradually becomes opaque as the

3. HIGH STRAIN RATE PROPERTIES OF EXPLOSIVES

J.E. Field, G.M. Swallowe, P.H. Pope and S.J.P. Palmer

Cavendish Laboratory, Madingley Road, Cambridge CB3 OHE

Abstract. Experiments are described on the deformation and ignition behaviour of a range of explosives, including some polymer bonded explosives (PBX's). An instrumented drop-weight apparatus was used to obtain stress-strain curves for strain rates in the range 10^2 to 10^3 s^{-1} . A novel drop-weight apparatus with transparent anvils allowed high-speed photographic recording of the impact and ignition processes. Laser speckle, used in conjunction with a specimen loaded in the Brazilian test geometry gave tensile strength and strain to failure data of PBX's. Finally, a modified Hopkinson bar apparatus gave data at strain rates up to $5 \times 10^4 \text{ s}^{-1}$.

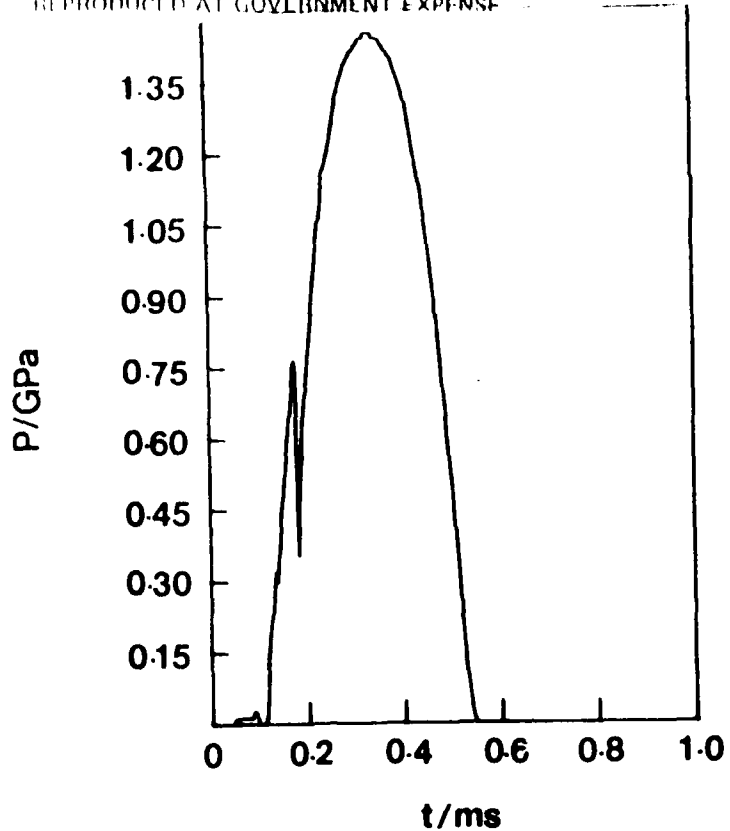
1. Introduction

It is generally accepted that explosive initiation is thermal in origin. In processes involving impact or shock, the mechanical energy is envisaged as being converted into heat in localized regions called "hot spots" (Bowden and Yoffe 1952, 1958) the required "hot spot" radius for ignition is a function of the explosive, the temperature and its duration (Rideal and Robertson, 1948). For pentaerythritol tetranitrate (PETN), the calculated "hot spot" temperature for a time of 1 μs and radius 1 μm is ca. 700 K. Experimental work by Bowden and Gurton (1949a,b) largely confirmed these figures and showed that "hot spot" radii are typically 0.1 to 10 μm for initiation by friction or impact. In a recent paper (Field et al, 1983) we have discussed the ignition mechanisms of explosives during mechanical deformation. Evidence was given for ignition by adiabatic heating of trapped gas, adiabatic shear of the explosive, friction, viscous flow, fracture or shear of added particles and triboluminescent discharge.

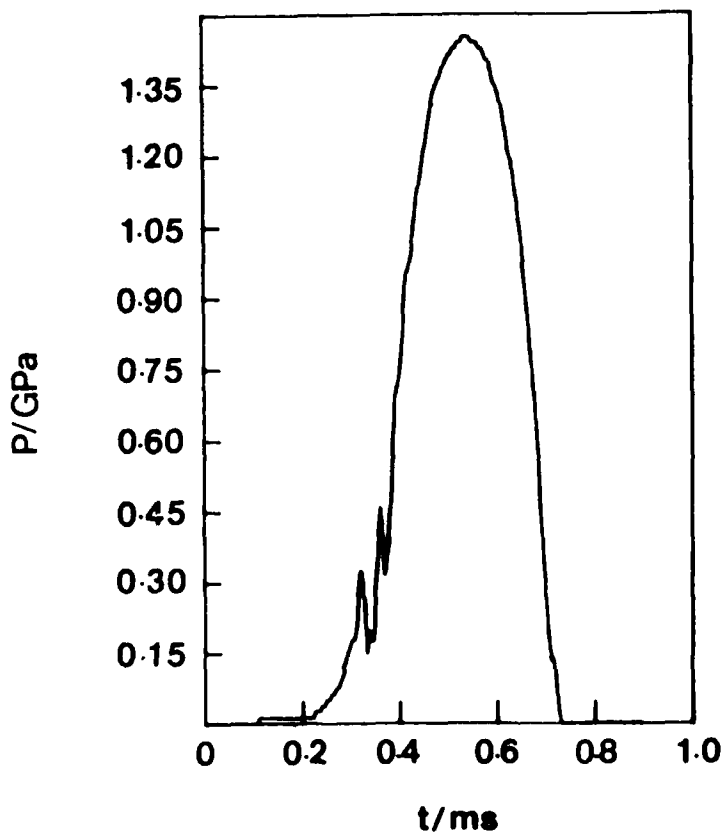
A feature of our work on the relation between mechanical properties and explosive behaviour has been the use of high-speed photography. The advantage of the photographic evidence is that it has allowed us to identify the conditions under which the various ignition mechanisms operate during deformation of an explosive.

In many modern applications, explosive crystals are bonded into a polymer matrix (so-called PBX explosives). It is important with such systems to understand the factors which affect their mechanical and thermal properties, their sensitiveness (response to a prescribed stimulus) and their explosiveness (explosive response). There is usually a conflict between these various requirements and an optimum has to be sought. The present paper describes results on pure explosives, explosives with additives and some PBX explosives based on cyclotetramethylene tetranitraramine (HMX).

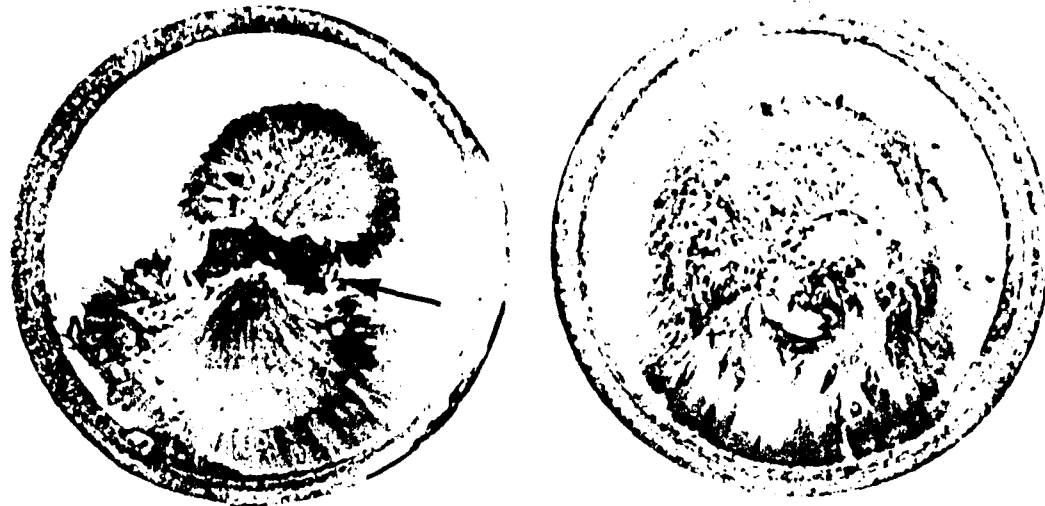
REPRODUCED AT GOVERNMENT EXPENSE



7(a)



7(b)



4

(a)

(b)

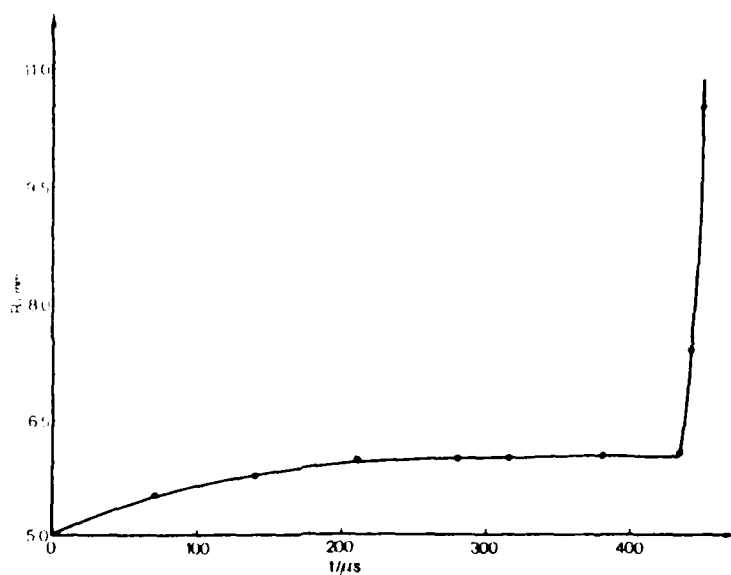
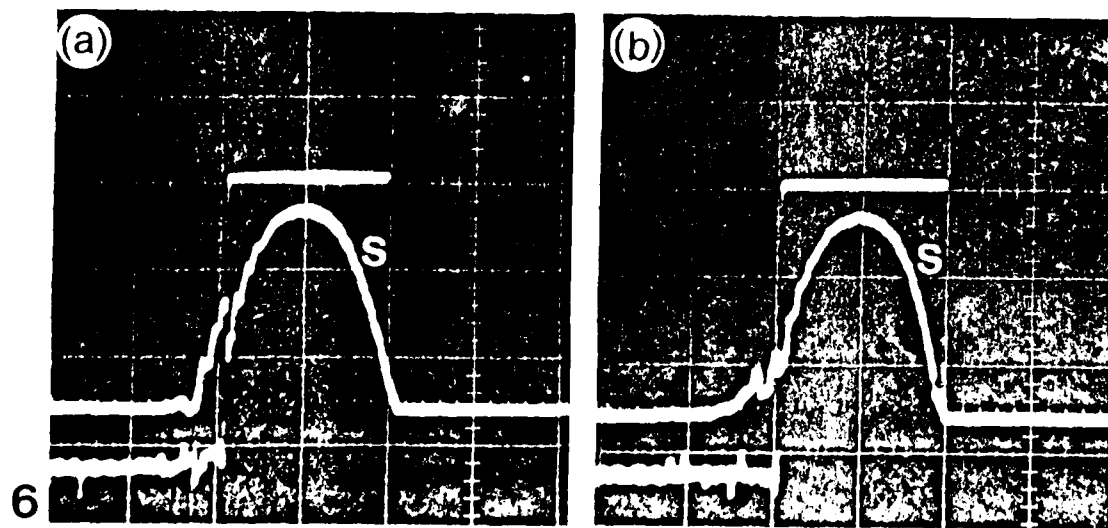


Fig. 5. Radius of a layer of HNS during impact showing evidence of plastic flow.



6

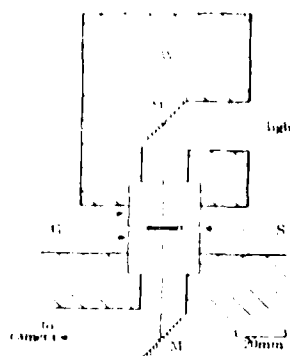


Fig. 1 Experimental arrangement at instant of impact; W, drop weight; G, glass blocks; M, mirror; S, sample. The upper glass block G is attached to the drop weight.

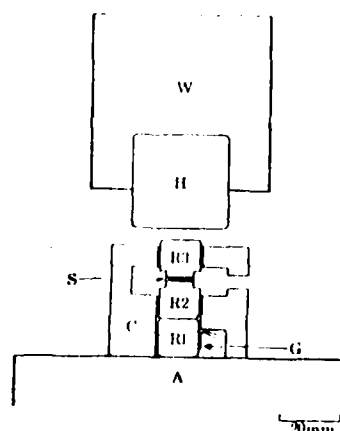


Fig. 2 Experimental arrangement for obtaining pressure-time curves; W, drop weight; H, R1, R2, and R3, hard steel rollers; C, cylindrical guiding sleeve; S, sample; G, strain gauge; A, cast steel anvil.

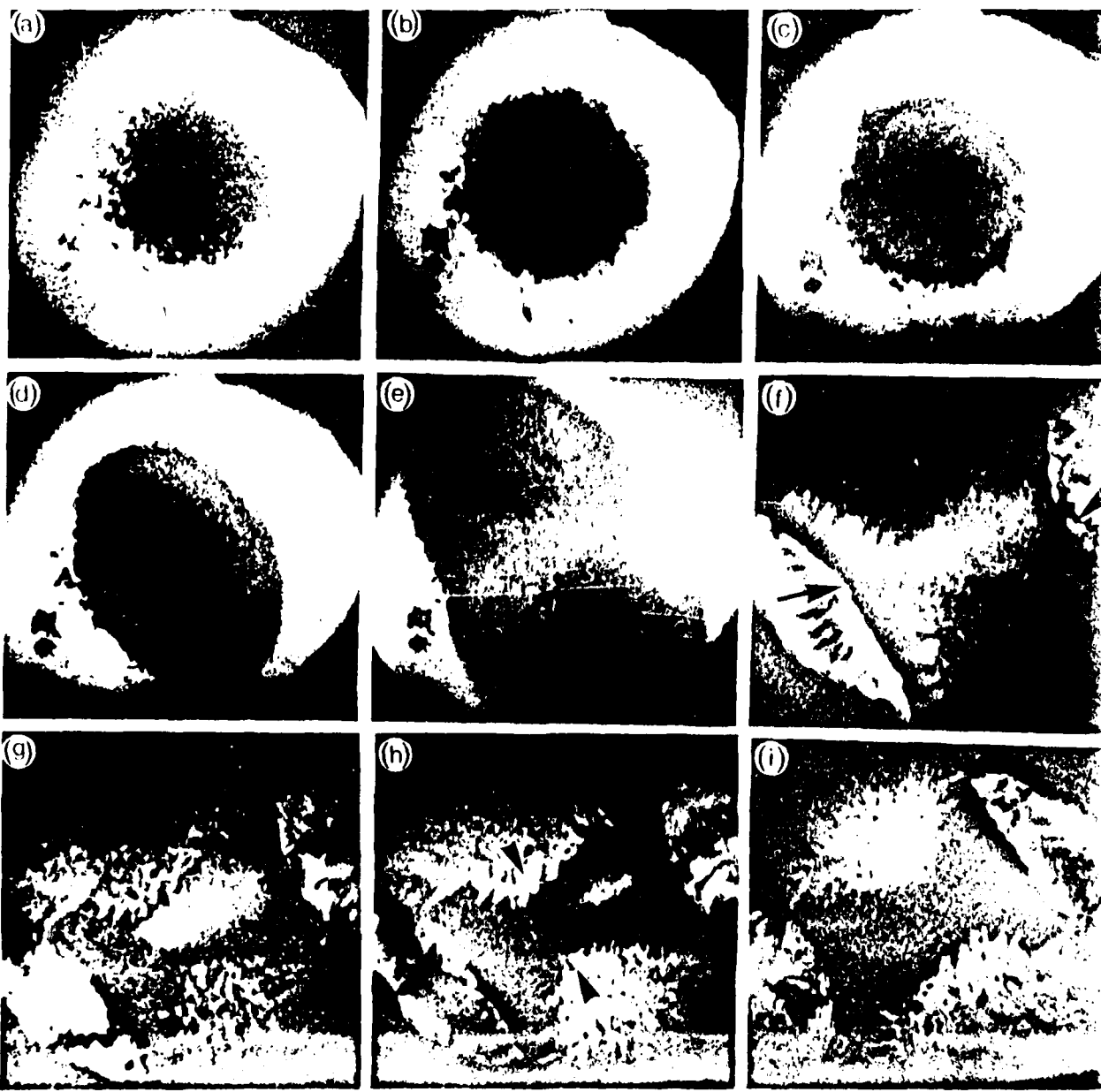


FIGURE LEGENDS

Figure 1 Experimental arrangement at instant of impact. W, drop weight; G, glass blocks; M, mirror; S, sample. The upper glass block G is attached to the drop weight.

Figure 2 Experimental arrangement for obtaining pressure-time curves. W, drop-weight; H, R12, R2, R3 hard steel rollers; C, cylindrical guiding sleeve; S, sample; G, strain gauge; A, cast steel anvil.

Figure 3 Impact on a layer of granular HNS. The sample becomes translucent [frame (d)] and starts to undergo plastic flow [frame (e)]. Ignition occurs in frame (f) at the periphery (see arrows). From frame (g) onwards fast reaction is taking place in the bright areas indicated by the arrows (see frame h). Frame time/ μ s : (a) 0; (b) 315; (c) 434; (d) 441; (e) 448; (f) 455; (g) 490; (h) 518 (i) 560.

Figure 4 Photograph of the toughened glass anvils after the impact test with (a) pure explosive (unreacted material indicated by an arrow) and (b) explosive/PC sample.

Figure 5 Radius of a layer of HNS during impact showing evidence of plastic flow.

Figure 6 Stress time curves for impact of (a) HNS and (b) HNS/PC. Mass of hammer 5 kg; drop height 1 m. The initially lower trace records the instant of ignition by monitoring the change in electrical resistance of the sample. The trace, labelled S, is the stress-time curve.

Figure 7 Pressure-time curves for impact of (a) HNS and (b) HNS/PC.

TABLE 2
 Strength properties and impact behaviour
 of various materials.

Compound	Melting point/K	Yield stress/MPa	H ₅₀ /m	Observations in impact apparatus
				Rapid flow Ignition
TNT	354 ^a	34 ^b	1.48 ^c	No ^d No
Picric acid	395	52	0.73	No No
Tetryl	404	53	0.37	No Yes ^e
PETN	414	60	0.13	Yes Yes
RDX	474	82	0.28	Yes Yes ^f
Ammonium				
perchlorate	>493	--	--	Yes Yes
HMX	553	125	0.32	Yes Yes
HNS	588	~ 140	0.54	Yes Yes
Potassium				
nitrate	>660	--	--	Yes --

- a. Values taken from Lawrence Livermore National Laboratory Explosives Handbook, UCRL-52997 (1981).
- b. All the yield stress values from ref. [10].
except for HNS which has been estimated using equation (3).
- c. Drop-weight 2.5 kg; sand paper surface. Data from reference given above in "a".
- d. The experimental observations for all compounds excluding tetryl and HNS are from ref. [1].
- e. Reaction fails to propagate.
- f. Ignition with large masses (100 mg) only.

TABLE 1

Infra-red absorption frequencies and
corresponding assignments for Hexanitrostilbene

Frequency/cm ⁻¹	Assignments
725 (s)	Aryl-CH-CH-Aryl out of plane deformation.
740 (s)	NO ₂ out of plane deformation; inconsistent band, limited value.
810 (s)	Aromatic (Ar)C-H out of plane deformation.
825 (s)	C-N Vibration; limited value.
920 (s)	Ar C-H out of plane deformation.
940 (s)	
955 (s)	Aryl-CH-CH-Aryl out of plane deformation.
1080 (m)	Ar C-H in plane deformation.
1340 (s)	Symmetric NO ₂ stretching.
1460 (b)	Ar C-C in plane deformation.
1535 (s)	Asymmetric NO ₂ stretching.
1600 (s)	Ar C=C in plane deformation.
1620 (m)	Ar C=C stretching.
3100 (s)	= C-H stretching.

Letters in parenthesis refer to the intensity of the band: s, sharp;
m, medium; b, broad.

REFERENCES

1. Heavens, S.N. and Field, J.E. Proc. Roy. Soc. (London) A338: 77 (1974).
2. Swallowe, G.M. and Field, J.E. Proc. Roy. Soc. (London) A379: 389 (1982).
3. Field, J.E., Swallowe, G.M. and Heavens, S.N. Proc. Roy. Soc. (London) A382 : 231 (1982).
4. Bowden, F.P., Mulcachy, M.F.R., Vines, R.G., and Yoffe, A.D. Proc. Roy. Soc. (London) A188 : 291 (1947).
5. Chaudhri, M.M. and Field, J.E. Proc. Roy. Soc. (London) A340 : 113 (1974).
6. Eirich, F.R. and Tabor, D. Proc. Camb. Phil. Soc. 44 : 566 (1948).
7. Bolkhovitinov, L.G. and Pokhil, P.F. Dokl. Akad. Nauk. SSSR. 123 : 637 (1958).
8. Bowden, F.P. and Yoffe, A.D. Fast reactions in solids, Butterworths, London, 1952.
9. Chaudhri, M.M. Nature (London) A263 : 121 (1976).
10. Afanasev, G.T. and Bobolev, V.K. Initiation of solid explosives by impact, Israel program for Scientific translations, Jerusalem, 1971.
11. Winter, R.E. and Field, J.E. Proc. Roy. Soc. (London) A343 : 399 (1975).
12. Frey, R.B. Proc. 7th Int. Symp. on Detonation, Office of Naval Research, Annapolis, Washington, D.C., 1981, p.36.
13. Kirshna Mohan, V. and Field, J.E. (unpublished results).
14. Schroeder, W. and Webster, D.A., J. Appl. Mech. 16 : 289 (1949).
15. Kholevo, N.A. Trudy. Kazan. Khim-tekhn. Inst. 10 : 91 (1946).
16. Tabor, D. Gases, Liquids and Solids, Cambridge University Press, Cambridge, 1971, p.207.
17. Windle, A.H., Phys. Bulletin 34 : 21 (1983).
18. Hagan, J.T. and Chaudhri, M.M. J. Mater. Sci. (Lett.) 12 : 1055 (1977).
19. Elban, W.L. and Armstrong, R.W. Proc. 7th Int. Symp. on Detonation, Office of Naval Research, Annapolis, Washington, D.C., 1981, p. 976.
20. Palmer, S.J.P and Field, J.E. Proc. Roy. Soc. (London) A383 : 399 (1982).

explosives which possess high strength are more susceptible to catastrophic failure and ignition during impact. This helps explain the behaviour of different materials in the drop-weight test and has important practical consequences for explosive formulations.

ACKNOWLEDGEMENTS

We thank Drs. M.M. Chaudhri and G.M. Swallowe for useful discussions and Mr. S.J.P. Palmer for help with the computer programmes.

cubic metals and semiconductors shows a qualitative correlation between these two quantities [17]. These facts suggest a link between the elastic moduli of a material, whose magnitude is to a large extent determined by the strength of the inter-atomic (or molecular) bonding forces, and the melting temperature which is another, albeit indirect, measure of such forces. Equation (3) is not valid in the case of secondary explosives because the units of crystal structures in such compounds are comprised of complex molecules, which, in turn, exhibit a vibrational complexity. However, for such secondaries, the uniaxial yield stress, which is another indicator of the mechanical strength of a solid is found to increase with the melting temperature of the explosive [10] (see Table 2). A similar trend is noticed in the hardness data for some of these explosives. For example, the Vickers hardness values, in units of kg/mm², for PETN, on its cleavage plane {110}, RDX, on the (210) growth surface, and β -HMX, on its cleavage plane {011}, are 17.9 (ref. 18), 35.2 (average of values given in ref. 19) and 40.3 (ref. 20), respectively, while the corresponding melting points are 414, 474 and 533 K. The hardness value for HNS is not known but it is reasonable to expect that it will be high. Young's modulus, uniaxial yield stress and Vickers hardness are related to each other by different expressions, see for example ref. [20]. Table 2 also gives the yield stress values and the impact characteristics such as flow properties and initiation of fast reaction for a number of explosives and also for potassium nitrate (which is a non-explosive compound). These data suggest that the strength of a compound in the drop-weight test is a key factor in determining the impact behaviour. If the strength is low, then deformation starts at a low stress and flow proceeds at moderate velocities. On the other if it is high, the onset of deformation is delayed but then develops catastrophically. Examples of flow at many hundreds of m s⁻¹ have been recorded in our work. Two important factors in the generation of 'hot-spots' are the rate of deformation and the resistance to this deformation. Thus it appears that

prerequisite for ignition is in agreement with those of Kholevo [15], Afanasev and Bobolev [10] and Heavens and Field [1]. As mentioned earlier the failure of the sample is rapid in nature.

Strength and sensitivity relation

A comparison of the flow properties for several explosives based on the results of Heavens and Field [1] and our work on HNS and tetryl [13] suggests that among organic secondary explosives, those with a high melting point normally exhibit a greater tendency to flow rapidly under impact. Thus trinitrotoluene (TNT), picric acid, and tetryl with melting points in the range 353-404 K show only minor deformation upon impact while explosives with high melting points such as RDX and HMX undergo bulk plastic flow in the glass impact apparatus. HNS is a high melting compound (melting temperature 588 K) therefore, the extensive flow seen in impact tests appears in line with previous results. The borderline for rapid flow in this equipment appears to lie between tetryl and PETN. The only other explosive studied which melts throughout the bulk is RDX, but then only between steel anvils [1,3].

For ionic solids with a simple cubic structure a semi-empirical relation, based on the Lindemann theory of vibrational instability of crystal lattices, can be derived between the melting temperature T and the Young's modulus E

$$T = \frac{E}{2\rho} \frac{M}{R} \beta^2 \quad (3)$$

where ρ is the density of the solid in kg/m^3 , M is the molar mass in kg and R is the gas constant in J/mol/K [16]. The vibration-amplitude x_0 when melting occurs is related to the atomic (or molecular) spacing, a, by $x_0 = \beta a$ with $0 < \beta < 1$. Although equation (3) is based on a crude model, it has yielded good agreement between the calculated and the observed melting points for several materials. Also, a plot of E versus T for a number of

impact apparatus, the reaction always proceeds to completion in this test. This is because the modulus and hardness of the steel used are greater than that of toughened glass. With HNS/PC two small incremental drops were recorded soon after impact and are attributed to the rapid deformation of the polymer.

The impact pressure, P , is given by the relation

$$P = \alpha U \quad (1)$$

where the constant α is the gauge calibration factor and U is the voltage signal from the gauge. The gauge was calibrated statically using an Instron machine and the calibration factor was found to be 0.043 GPa/mV. The pressure-time curves obtained using equation (1) are presented in Fig. 7. At first the sample is compressed and compacted. Eventually the strength of the layer is exceeded and the material deforms plastically. In the drop-weight test the average pressure for yield, P_{ult} , is higher than the uniaxial yield stress of the material σ_y . This is due to the constraining effect of the anvils. Application of the Mises yield criterion to a thin layer of thickness h and diameter d between two rigid cylindrical punches gives the following hyperbolic expression [14].

$$P_{ult} = \sigma_y [1 + (d/3\sqrt{3} h)] \quad (2)$$

Note that, the smaller the thickness, or greater the diameter, the higher the value of P_{ult} . From Fig. 7 it can be seen that P_{ult} value for HNS under the test conditions is 760 MPa. For HNS/PC two pressure drops are recorded; the lower values for the explosive/polymer sample suggesting that they correspond to the failure of PC. Using equation (2), an approximate value for the yield stress of HNS can be estimated. σ_y is thus found to be 140 MPa.

For HNS both the impact photographs and the stress-time curves show that there is a close relation between the mechanical failure of the layer and the instant of ignition; the ignition always occurring either during or after the failure. Our observation that rapid deformation is a necessary

under impact is 'partial'. Swallowe and Field [2] have examined in detail the effect of a number of polymers on the H_{50} values of the secondary explosives, PETN and HMX. These authors found that some relatively soft, low-melting polymers such as PC and polysulphone (PSu) can also sensitize explosives. These polymers fail catastrophically either by fracture or localized adiabatic shear and have a low specific heat, latent heat and thermal conductivity. The temperature of the 'hot' spots in such polymers, produced during rapid deformation, can greatly exceed the polymer's softening point. Neither the size of the grit nor the percentage content in the explosive/grit mixture were seen to influence the extent of sensitization. For HMX, addition of PC reduced the H_{50} values from 29.0 ± 2.0 cm (for the pure compound) to 16.0 ± 1.5 cm [2]. The sensitization is due to 'hot spots' generated by non-homogeneous energy dissipation either in adiabatic shear bands or at crack tips in the polymer. In the current work the effect of PC on the impact initiation of HNS was investigated. In three trials with HNS/PC samples between glass anvils, explosion always propagated to completion with no explosive remaining on the anvils. The bottom anvil from one such trial is shown in Fig. 4(b). In the steel impact apparatus, the H_{50} value of the pure explosive decreased from 0.68 ± 0.02 m to 0.40 ± 0.03 m in the presence of the polymer.

Impact behaviour in the drop-weight test

The stress-time curves for pure HNS and HNS/PC were obtained using an instrumented drop-weight machine with steel anvils and are presented in Fig. 6(a) and (b) respectively. The trace (marked S) represents the stress-time relation recorded by the strain gauge during impact and the lower trace detects the instant of ignition by recording a jump in the electrical conductivity of the material between the anvils. For the pure explosive, the prominent feature of Fig. 6 (a) is a sharp break in the stress-time curve associated with ignition following mechanical failure of the sample. Contrary to the 'partial' nature of reaction in the glass

explosion propagates further. The transition from a translucent to an opaque layer is thought to be due to the fact that the gaseous explosion products separate the impacting anvils slightly and reduce the impact pressure. The photographs also show that the fast reaction does not propagate into the centre of the sample. In fact, examination of the bottom anvil after the test indicates that a certain amount of explosive remains behind. The anvil is shown in Fig. 4(a). In order to ascertain that the residue is unreacted explosive rather than partially decomposed material, its infra-red spectrum was taken in Nujol and compared with that of pure HNS. The two spectra were found to be identical thus confirming that the material on the anvil was unreacted HNS. The principal infra-red absorption frequencies and the respective assignments are listed in Table 1.

The photographic work described above establishes that the mechanical response of a thin layer of HNS to impact is characterized by a large scale deformation process prior to initiation of explosion. As mentioned in the Introduction, similar processes are also observed in PETN, RDX and HMX. With PETN, the material becomes translucent and finally completely transparent with rapid flow (300 m s^{-1}) which was attributed to melting [1]. With HNS too, high flow speeds were recorded. A graphical illustration of the effect of mechanical failure of the sample on its flow is provided by Fig. 5 in which the radius of the explosive is plotted as a function of time for the sequence of Fig. 3. During the early stages of compression up to $100 \mu\text{s}$ the material spreads uniformly at 10 m s^{-1} and then the bulk of it ceases to flow till ca. $430 \mu\text{s}$. Next there is a sudden increase in the rate of flow from zero to over 250 m s^{-1} . During the flow the layer takes an elliptical shape and the 'radius' now refers to the major axis of the ellipse. Initiation of explosion occurs only after this rapid plastic flow.

As evident from impact photographs and Fig. 4(a), explosion of HNS

2. Experimental

Experiments have been carried out using the drop-weight machines illustrated in figures 1 and 2. The samples used are 5 to 7mm in diameter and 1mm high allowing strain rates of 10^2 to 10^3 s^{-1} to be obtained, depending on the drop-height of the weight. In both machines the weight is guided by three cylindrical rods. Figure 1 illustrates the system which is used to obtain stress-strain curves. Strain gauges attached to r_1 allow the force-time history to be monitored. The area of deforming sample is determined by r_2 and r_3 and the sample size is chosen to be, initially, slightly greater than this area. The sample area under load is thus constant and the need for assumptions about volume conservation, which are not always valid for polymers or porous materials, is eliminated. Knowledge of the mass of the weight combined with a double integration of the force-time data produces force-displacement information which is then converted to a stress-strain curve. The system illustrated in figure 2 is unusual in that the anvils are made of toughened glass and a light path through the system allows the sample to be photographed by a high speed camera at framing rates up to $2 \times 10^5\text{ f.p.s.}$ during the course of the impact. The sample strain-rates in both machines are the same so that direct comparisons between the photographic records and the stress-strain data can be carried out.

The third system used in this research was a miniaturised and modified Hopkinson bar apparatus (as described by Gorham, 1979). This enabled measurements to be made, and stress-strain curves determined, at strain rates up to $5 \times 10^4\text{ s}^{-1}$. The samples used in these experiments are 4mm diameter and 1mm thick, and the pressure bar has a diameter of 3mm.

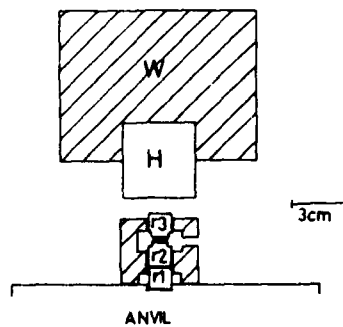


Fig. 1 Instrumented drop-weight:
W, drop-weight; H, r_1 , r_2 , r_3 ,
hardened steel rollers. The sample
is between rollers r_2 and r_3 .

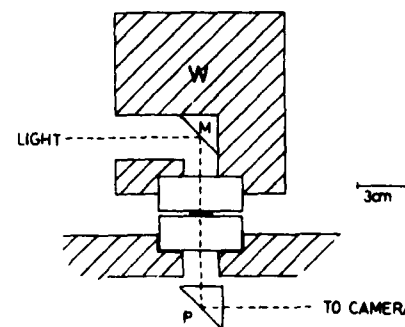


Fig. 2 Experimental arrangement at
instant of impact: W, drop-weight
(5.5 kg); G, glass blocks; M, mirror
P, prism; S, sample.

Finally, the tensile strengths and rupture strains of a variety of PBX compositions were studied, at strain rates of ca. 10^{-4} s^{-1} , using the 'Brazilian' test geometry and laser speckle photography. The Brazilian test is illustrated in figure 3. The compression induces tensile stresses normal to the loading axis which are sensibly constant over a region about the centre of the specimen. The tensile strength of the material is then calculated from

$$\sigma_t = 2P/\pi D t$$

1

in which P is the failure load, D and t the diameter and thickness of the specimen respectively. The validity of equation 1 is based on the assumptions that failure occurs at the point of maximum tensile stress

(i.e., at the centre), and that the compressive stress has no influence on the failure (Fairhurst, 1964). In practice, the use of plane anvils can produce very high contact stresses at the loading points, and lead to the collapse of the contact edge. Awaji and Sata (1979) have shown that by using curved anvils, collapse of the edge can be avoided, and shear stresses under the points of loading may be substantially reduced. It has been shown by Awaji and Sata that if the ratio of the contact half-width, b , to the disc radius, R , is larger than approximately 0.27, the maximum principle stresses near the contact area are compressive. Then the stresses near the centre of the disc control the fracture, and cracking occurs at the centre, at a maximum tensile stress given by

$$\sigma_t^* = \{1 - (b/R)^2\} \sigma_t \dots \quad 2$$

The use of strain-gauges to measure the tensile strain to failure of the PBX compositions have several disadvantages. These materials are relatively soft and the gauge may reinforce the material at the point where the strain is to be measured. Furthermore, once installed, it can only provide information at one point. An alternative approach is to use an optical technique which measures in-plane surface displacements. Laser speckle photography is a simple remote-sensing technique, in which in-plane displacements can be determined, with a high sensitivity Chiang (1982). For displacement and strain measurements, a double exposure is photographically recorded before and after deformation. The negative then consists of two identical speckle patterns that have been translated with respect to each other. Displacement information can be extracted in a point-wise manner, by allowing an unexpanded laser beam to pass through the negative. If at the point illuminated by the beam, the 'speckles' have been displaced between exposures, the resulting displacement vector is manifested by a Young's fringe pattern observed on a screen placed at the far-field Fraunhofer diffraction plane. The displacement vector is perpendicular to the fringe orientation and the magnitude inversely proportional to the fringe spacing. Figure 4 shows a speckle pattern being processed.

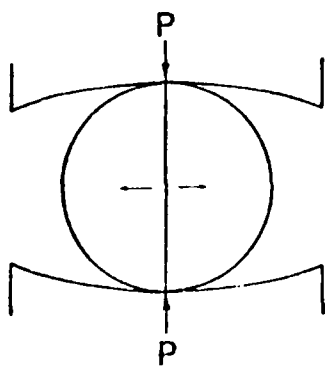
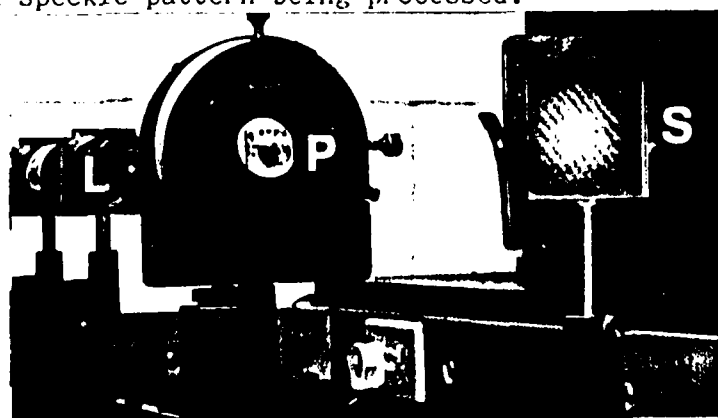


Fig. 3 Loading arrangement used in Brazilian test.



laser, L, passes through the speckle pattern, P, and forms a Young's fringe pattern at the screen S.

3. Results

3.1 Pure Explosive

Figure 5 shows an impact on PETN taken using the system of figure 2. At first the sample is compressed and compacted, and its radial expansion is at a similar velocity to that of impact (i.e. a few m s^{-1}). This stage is not illustrated. Eventually the strength of the layer is exceeded and the

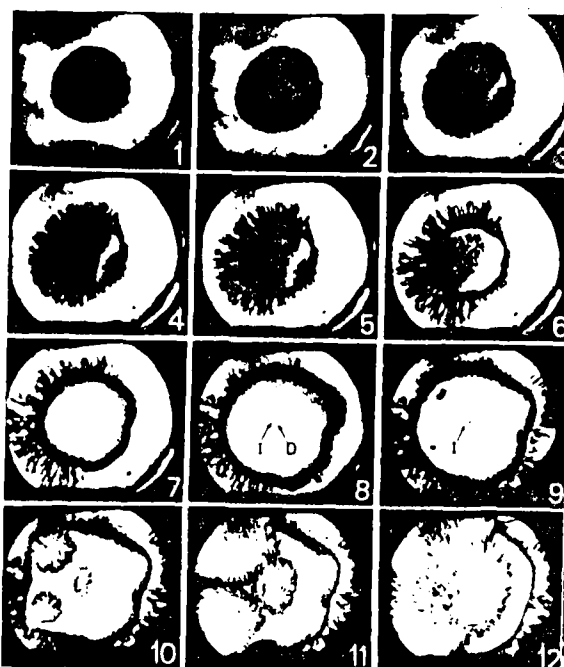


Fig. 5 Impact on a layer of PETH. The sample flows plastically, melts and ignites at a number of sites. In frames 7, 8 and 9 f is a flaw in the glass and I is an ignition site. Sample mass is 14 μg , inter-frame time 5.5 μs .

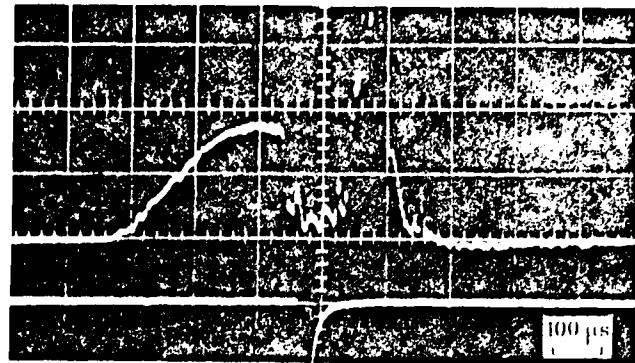


Fig. 6 (a) Top: pressure-time trace for an RDX sample. The lower trace records the instant of ignition.

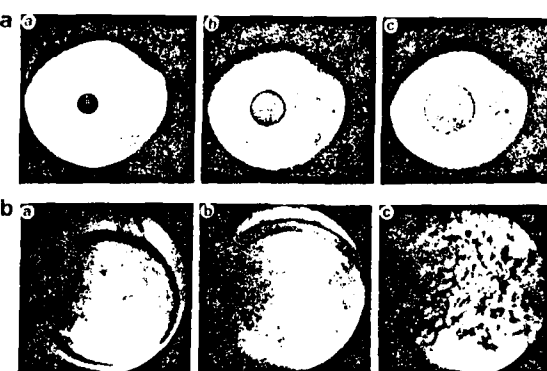


Fig. 7: (a) Impact on a disc of IP. The sample deforms by bulk plastic flow. Frame times μs : a, 0; b, 76; c, 266. Field of view 20 mm.
 (b) Impact on a disc of PS. The sample fails catastrophically (c). Frame times μs : a, 0; b, 21; c, 28. Field of view 2.5 mm.

material deforms plastically. It is important to realize that in this loading geometry the stress for yield σ_y is higher than the uniaxial yield stress of the material σ_y . This is due to the constraining effect of the anvils. Application of the Mises yield criterion to a thin layer of thickness h and diameter d between two rigid cylindrical punches gives the following relation (Schroeder and Webster 1949)

$$\sigma_y = \sigma_{y0} [1 + (d/3\sqrt{3}h)]$$

3

Note that, the smaller the thickness, or the greater the diameter, the higher the value for σ_y . Once plastic flow results, the radial expansion of the layer can be rapid (more than 100 m s^{-1}). In explosive samples without additives, ignition invariably occurs after this rapid deformation. This fact, taken in conjunction with equation 3, explains many of the sample size effects found in impact ignition (for a fuller discussion see Heavens and Field 1974; Gaudini and Field 1977). Note that, though ignition occurs after rapid flow, rapid flow does not necessarily cause ignition. We have frequently observed samples that deformed rapidly but that did not ignite. The rapid flow following plastic deformation occurs in frames (b) onwards. It will be noted that for PETH the layer becomes transparent, and flows very rapidly (100 m s^{-1}) before ignition. This transparency is due to the layer melting. We have evidence of similar behavior with cyclotrimethylenetrinitramine (RDX). With ammonium perchlorate (AP) the

layer also goes transparent, but this is not due to fusion but to sintering of particles. Evidence for this is that a similar transparency can be achieved in AP by static loading, the transparency during impact occurs before the plastic flow and is partially lost during the plastic deformation stage, and that once ignition occurs fractures can be detected in the material ahead of the burning front (see figure 4, Heavens and Field 1974). The observation that rapid deformation is a necessary prerequisite for ignition supports the many observations of Kholevo (1946) and Afanas'ev and Bobolev (1971) that the prevention of flow in an explosive sample makes the sample less sensitive. Further support for this view is provided by the stress-time traces obtained with the instrumented drop-weight machine. Results for impacts on a wide range of explosive and inert layers have been presented before (Heavens and Field 1974). A typical result is reproduced in figure 6. The upper trace represents the stress-time relation recorded by the gauges during an impact on a layer of RDX, and the lower trace detects the instant of explosion by recording the light output with a photocell. This result shows clearly the very close relation between mechanical failure of the layer and the instant of ignition, the ignition always occurring during or after the failure.

TABLE 1

Compound	Melting point/K	Yield stress/MPa	H_{50}/m	Rapid flow	Ignition
TNT	354	34 ^a	1.48 ^b	No ^c	No
Picric acid	395	52	0.73	No	No
Tetryl	404	53	0.37	No	Yes ^d
Nitrocellulose	408	-	0.50	No	Yes ^d
PETN	414	60	0.13	Yes	Yes
RDX	474	82	0.28	Yes	Yes
AP	>493	-	-	Yes	Yes
HMX	553	125	0.32	Yes	Yes
HNS	588	-140	0.54	Yes	Yes

a. All the yield stress values have been taken from Afanas'ev and Bobolev (1971) except for HNS (estimated by Krishna Mohan and Field (1984)).

b. Data from Lawrence Livermore Explosives Handbook, UCRL-52997 (1981).

c. The experimental observations for all compounds excluding tetryl and HNS are from Heavens and Field (1974).

d. Reaction fails to propagate.

Recently we have shown that the higher the yield stress of a pure explosive the higher its plastic flow velocity in the drop-weight test. Thus although with a strong sample the onset of irreversible deformation is delayed it eventually develops more rapidly when the stored energy is released. This means that the likelihood of ignition during the conversion of mechanical energy is greater. Table 1 illustrates these results and explains why a relatively soft, low melting point explosive, such as trinitrotoluene (TNT) does not ignite so readily in the drop-weight test. A fuller discussion can be found in Krishna Mohan and Field (1984).

3.2 Explosives with Polymer Additives

Certain polymers, when mixed with explosives, cause them to have a higher sensitiveness to impact (Swallowe and Field 1981, 1982). The evidence

suggests it is not due to chemical effects but is related to the polymers thermal properties and mode of deformation which both affect the 'hot-spot' formation. Polymers that sensitize are those that are relatively tough, but that when they fail do so catastrophically with the energy dissipation either in adiabatic shear bands or at crack tips. Such polymers include polycarbonate (PC), polysulphone (PS) and polyester (PE). These materials all have low thermal conductivities and latent heats of fusion which allow 'hot-spot' temperatures to reach much greater values than that of the softening point. Conversely, polymers such as polypropylene (PP), which deform in a bulk fashion and which have relatively high conductivities and latent heats have 'hot-spot' temperatures 'quenched' to the melting-point value. Figure 7 illustrates the different deformation modes of PP and PC during impact in the drop-weight machine. Figure 8 illustrates their stress/strain curves, found using the apparatus shown in figure 1. The almost vertical drop in the curve for PC is due to the catastrophic failure illustrated in figure 7b.

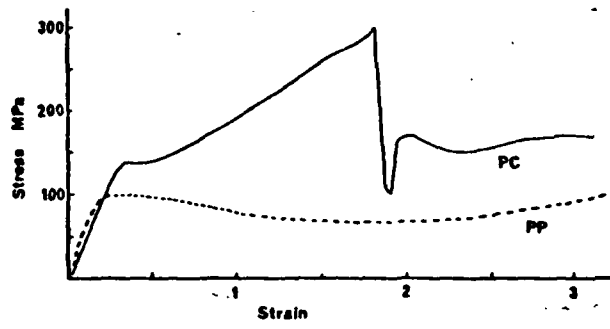


Fig. 8 Stress-strain curves for samples of PP and PC. Catastrophic failure of the PC sample occurs at a strain of ca. 1.8.

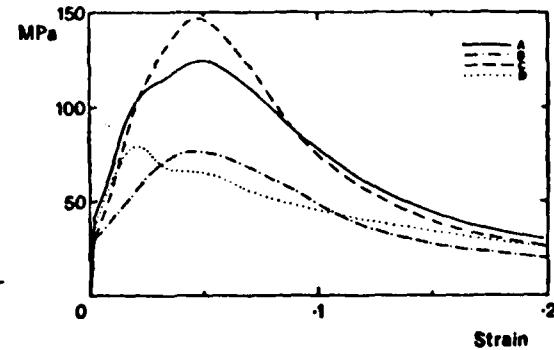


Fig. 9 Stress-strain curves for compositions A, B, C, D, at a strain rate of $2.5 \times 10^4 \text{ s}^{-1}$.

3.3 PBX's

Table 2 gives information on the PBX's studied. They were all based on HMX but with three different binder polymers. The amount of binder and the crystal size distributions of the HMX were varied. Included in Table 2 are the results on the strain to failure and the failure stress obtained using the speckle technique. Various general points can be made (i) micronized samples are stronger (ii) the more the polymer the greater the strain to failure (iii) PE gives the most brittle behaviour (lowest strain to failure) followed by Viton and PU. (iv) composition C had the highest combination of strength and strain to failure. Figure 9 and Table 3 summarize results on the PU-compositions from the high rate of strain experiments ($\epsilon = 2.5 \times 10^4 \text{ s}^{-1}$). Note that the sample with micronized HMX exhibit the highest dynamic strengths, with C again proving the strongest. Table 3 also contains F of I and labset figures. The micronized samples (A,C) had smaller labset (explosiveness) values. This was also found with the other binder materials. Figures 10 and 11 show photographic records of impacts on compositions B and C. The micronized PBX (composition C) burns smoothly and rapidly but leaves a large amount of residue. The sample of composition B shows extensive break up. The production of large internal surfaces and the rapid penetration of burning into them leads to a more violent and complete explosion (less residue in these tests). This probably explains the higher labset value.

TABLE 2

Code	Binder	% binder by weight	HMX	% strain to failure	Failure stress/ MPa. b/R = 0.27
A		2	M	0.95	1.38
B	Polyurethane	2	A/M	0.50	1.22
C	(PU)	5	M	0.98	3.20
D		5	A/M	1.24	0.99
E		2	M	ca. 0.06	3.11
F	Polyethylene	2	A/M	0.09	0.67
G	(PE)	5	M	internal shear -	-
H		5	A/M	0.18	0.56
I		4	M	0.24	1.89
J	Viton	4	A/M	0.32	1.14
K		9	M	0.31	1.99
L		9	A/M	0.41	0.89

M. Micronized (to pass 53 μ m sieve)

A. Size range 50 - 1000 μ m, median diameter ca. 400 μ m. A/M. Ratio 63/35.

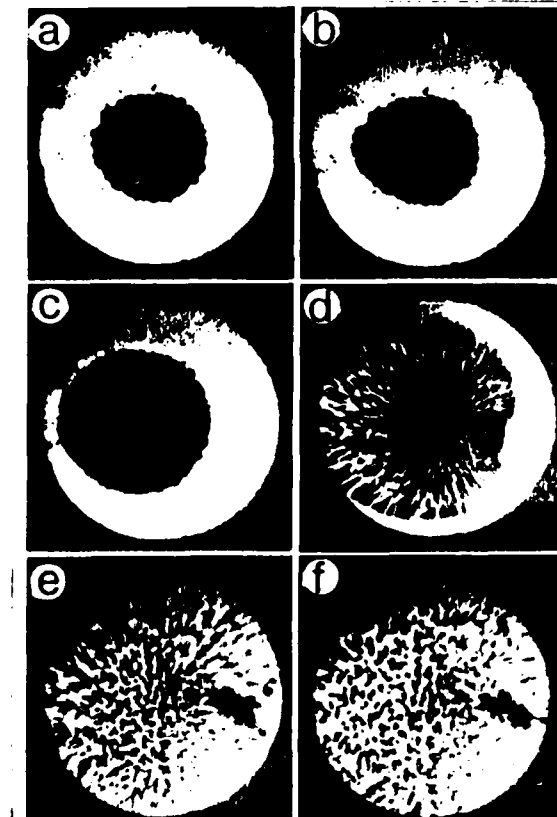


Fig. 10 Impact on a sample of composition C. The sample undergoes rapid flow (frame b and c) and ignition occurs at numerous sites throughout the sample. (frame e and f). A larger amount of unconsumed material remained at the end of the test. Interframe times b to f 7 μ s. Field of view 20 mm.

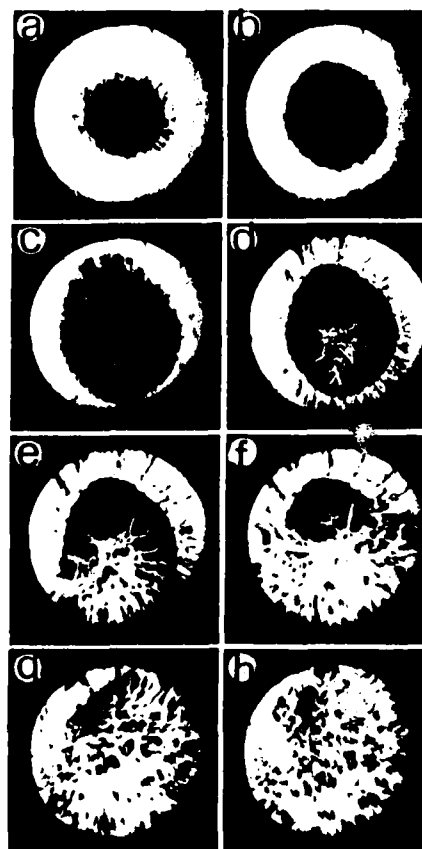


Fig. 11 Impact on composition B which undergoes rapid flow (b and c) and ignites. Extensive break-up with the production of internal surfaces aids reaction. Interframe times b to h 7 μ s. Field of view 20 mm.

TABLE 3

Code	Dynamic strength ($2.5 \times 10^4 \text{ s}^{-1}$)/MPa	F of I ^a	Labset ^b
A	125	62	185
B	80	64	812
C	145	55	58
D	85	49	232

a. Figure of Insensitiveness, based on a drop-height for RDX of 80. The greater the figure the less the sensitiveness (AWRE data).

b. Labset is the AWRE test for explosiveness. The greater the figure the greater the explosive response (see Coley, 1976).

4. Conclusion

The combination of techniques used in this study has provided valuable information on the mechanical and ignition behaviour of explosives. The techniques themselves have application to deformation studies of materials in general.

5. Acknowledgements

This work was supported in part by the Ministry of Defence (Procurement Executive) and Grants through the European Office of U.S. Research.

REFERENCES

Afanas'ev, G.T. and Bobolev, V.K. 1971 Initiation of solid explosives by impact. Jerusalem: Israel Program for Scientific Translations.

Awaji, H. and Sata, S. 1979 J. of Engng., Mat. and Tech., 101, 140.

Bowden, F.P. and Gurton, O.A. 1949a Proc. Roy. Soc. London A198, 337.

Bowden, F.P. and Gurton, O.A. 1949b Proc. Roy. Soc. London A198, 350.

Bowden F.P. and Yoffe, A.D. 1952 Initiation and Growth of Explosions in Liquids and Solids. Cambridge University Press.

Bowden, F.P. and Yoffe, A.D. 1958 Fast Reactions in Solids. London: Butterworths.

Chiang, F.P., 1982, Opt. Engng., 21, 379.

Coley, G.D. 1976, Proc. Sixth Int. Symp. Detonation, O.N.R. p. 290.

Fairhurst, C. 1964. Int. J. Rock Mech. Mining Sci., 1, 535.

Field, J.E., Swallowe, G.M. and Heavens, S.N. 1983, Proc. Roy. Soc. London, A382, 231.

Gorham, D.A., 1979, Inst. Phys. Conf. Series, 47, p. 16.

Heavens, S.N. and Field, J.E. 1974 Proc. Roy. Soc. London. A338, 77.

Kholevo, N.A. 1946, Trudy Kazan Khim.-Tech. Inst. 10, 91.

Schroeder, W. and Webster, D.A. 1949, J. Appl. Mech. 16, 289.

Swallowe, G.M. & Field, J.E. 1981, Proc. 7th Int. Symp. Det., O.N.R. p.24.

Swallowe, G.M. and Field, J.E. 1982, Proc. Roy. Soc. London A379, 389.

4. Thermal, Fracture and Laser-induced Decomposition of PETN

W.L. Ng*, J.E. Field, H.M. Hauser⁺

Cavendish Laboratory
Madingley Road
Cambridge
CB3 OHE

ABSTRACT

This paper describes a study of the decomposition of pentaerythritol tetranitrate (PETN) using a high-resolution time-of-flight mass spectrometer. The decomposition was induced by fracturing single crystals and by laser irradiation. In the fracture experiments, the energy input was varied from the lowest level necessary to produce smooth cleavage surfaces to high energy loading which produced rough conchoidal fracture surfaces. In the laser experiments, a ruby laser was used in both normal and Q-switched modes, and again the energy input was varied. For all the various experiments, the reaction products were analysed and reaction schemes are proposed. It is shown that low energy fracture causes decomposition which follows the same reaction pathway as that induced thermally, with initial failure at the RO-NO₂ bond. However, high energy fracture results in the breaking of the C-C bonds. Two reaction pathways were observed with the laser irradiation. The first is the normal thermal process, but evidence was also found for failure at the R-ONO₂ bond. The reaction continued for several milliseconds after the end of the laser pulse suggesting a 'partial' ignition of the explosive. In other experiments, the conditions for laser initiation of PETN in vacuum were investigated. Explosion occurred when Q-switched pulses of 1 J energy were applied to a molten layer of PETN.

* Now at: Department of Chemistry, University of Malaya, Kuala Lumpur, Malaysia.

+ Now at: Acorn Ltd., Fulbourne Road, Cambridge.

1 INTRODUCTION

Pentaerythritol tetranitrate (PETN) is a widely used secondary explosive. Its relatively high chemical stability allows it to be manufactured, handled and stored in comparative safety. Its thermal decomposition has been the subject of intensive study, and results on the energies involved and the reaction pathway are summarised below in section 2. Such decomposition has relevance to the long-time storage of PETN and to situations involving relatively slow thermal inputs. However, there is no certainty that the same reaction pathways will operate when fast decomposition at transient 'hot spots' takes place.

It is now generally accepted that explosives almost invariably ignite by thermal processes (Bowden and Yoffe 1952, 1958). The energy input may be directly thermal or may involve the degradation of mechanical energy into local 'hot spots' (see Field, Swallowe and Heavens 1983, for a recent review). Whether or not fast reaction develops from the 'hot spot' then depends on the balance of heat produced by chemical reaction and that lost by dissipative processes.

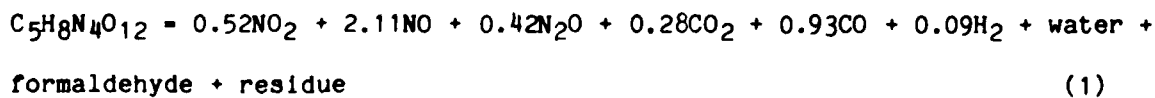
The object of the present research was to investigate the decomposition pathways for PETN following the production of transient 'hot spots', and to compare the results with those obtained from slow thermal decomposition studies. In one set of experiments, crystals were fractured in a variety of ways; in this situation the 'hot spot' forms at the tip of the running crack (see Field et al (1982) for a discussion). Direct measurements of crack tip temperatures, which may reach several hundred K have been made by Doll (1973), Fuller, Fox and Field (1975) and Weichert and Schonert (1974). In other experiments, a ruby laser was used to produce a transient 'hot spot' in the material. The experiments were performed in an ultra-high vacuum system with a time-of-flight (TOF) mass spectrometer used to detect and analyse the transient species and the decomposition products. A

preliminary account of the fracture experiments was given in Hauser, Field and Krishna Mohan (1983).

Finally, the conditions under which PETN initiates in vacuum when irradiated by a ruby laser pulse were investigated.

2 THERMAL DECOMPOSITION

Andrews and Kaidymov (1961) found an activation energy E of 215 to 263 kJ mol⁻¹ for the decomposition of solid PETN but their result was based on a limited amount of data. Values from other workers using a variety of methods fall reasonably close together. Rogers and Morris (1966) using differential scanning calorimetry (DSC) found a value of 198 kJ mol⁻¹. Soria-Ruiz (1969) obtained 176 kJ mol⁻¹ by monitoring the peak m/e 28 using a quadrapole mass spectrometer. Ng, Field and Hauser (1976), measuring the total gas evolution, found a value of 192 kJ mol⁻¹. Vapor phase decomposition was studied by Robertson (1948) who found an activation energy of 197 kJ mol⁻¹ while Maycock and Verneker (1970) using a thermobarogravimetric technique obtained 188 kJ mol⁻¹. Decomposition is complex and takes place concurrently with sublimation. Decomposition products at 483 K were analysed chemically by Rideal and Robertson (1948) who found



This was supported by the time-of-flight mass spectrometry study of Ng et al (1976) who found that the product distribution is temperature sensitive. The activation energy for decomposition is close to the bond dissociation energy of ca. 173 kJ mol⁻¹ for RO-NO₂ in mononitrate and nitrite esters estimated by Levy (1954). A mechanism was proposed by Ng et al (1976) for the thermal decomposition of PETN via the rupture of the RO-NO₂ bond

followed by the elimination of a neutral formaldehyde molecule as given below:

Normal Thermal Decomposition Pathway

$\text{C}(\text{CH}_2\text{ONO}_2)_4$	\rightarrow	$\text{C}(\text{CH}_2\text{ONO}_2)_3\text{CH}_2\text{O} + \text{NO}_2$	2
$\text{C}(\text{CH}_2\text{ONO}_2)_3\text{CH}_2\text{O}$	\rightarrow	$\cdot\text{C}(\text{CH}_2\text{ONO}_2)_3 + \text{HCHO}$	3
$\cdot\text{C}(\text{CH}_2\text{ONO}_2)_3$	\rightarrow	$2\text{CH}_3\text{ONO}_2 + 2\text{CO} + \text{NO}$	4
CH_3ONO_2	\rightarrow	$\text{CH}_3\text{O} + \text{NO}_2$	5
$\text{CH}_3\text{O} + \text{NO}_2$	\rightarrow	$\text{HCHO} + \text{HONO}$	6
2HONO	\rightarrow	$\text{H}_2\text{O} + \text{NO} + \text{NO}_2$	7
$\text{CH}_3\text{O} + \text{HCHO}$	\rightarrow	$\text{CH}_3\text{OH} + \text{HCO}$	8
$\text{HCO} + \text{NO}$	\rightarrow	$\text{CO} + \text{HNO}$	9
2HNO	\rightarrow	$\text{H}_2\text{O} + \text{N}_2\text{O}$	10

3 EXPERIMENTAL

PETN in powder form was obtained from PERME, Waltham Abbey. Large single crystals (typically $20 \times 5 \times 3 \text{ mm}^3$) were grown from acetone solution. The crystals were prismatic with elongated hexagonal (100) planes. They were mounted on a movable platform inside a six-way reaction chamber of an ultra-high vacuum (UHV) system connected to a Bendix RGA-1A time-of-flight mass spectrometer. A view of the experimental arrangement is given in figure 1. The sample was within 40 mm of the ion source which was operated at 70 V.

A trace offset controller was used to present a step-wise display of the mass spectra on a Tetrotronix oscilloscope (model A7603). It is capable of displaying a maximum number of 64 spectra in 8 steps on a single oscilloscope. The sweep time for each spectrum is 33 μs . It also has a horizontal offset component to displace the steps sidewise relative to each other so as to avoid overlapping of high rising peaks between adjacent steps. A built-in time delay unit on the oscilloscope trace offset

controller is adjustable between $4\mu\text{s}$ and 1 ms. An additional time delay circuit was designed (Hauser 1977) to extend and vary the delay time between 40 ms and 3 s. A high-writing speed camera, C27, using polaroid film was used to record the oscillograms. An oscilloscope bright-up unit was also used to facilitate easy data acquisition.

a) Fracture Induced Decomposition

A chisel was mounted on a metal bellows assembly situated on the top compartment of a six-way reaction vessel. Its shaft had a hollow section to accommodate a small explosive fuse. The platform on which the sample was placed could be raised towards the stationary chisel edge by means of a linear motion device (LMD) mounted in the compartment opposite to the chisel. When the crystal surface was just touching the chisel edge, two modes of initiating a fracture were then carried out.

i) Less energetic fracture

The chisel edge was aligned parallel to a (110) cleavage plane of the crystal via a rotating flange to which the LMD was attached (figure 2a). This could be achieved by rotating the entire LMD assembly until the edge of the chisel was parallel to the long edge of the crystal. The crystal was loaded against the chisel by raising the platform until the crystal cleaved. This process was carried out slowly so that the minimum cleavage force was used. A spectrum was taken as soon after cleavage as possible. The estimated time delay between the event and the recording was ca. 1 s.

ii) Energetic fracture

In this situation, the crystal was not orientated preferentially and excess energy was rapidly fed into the chisel by firing an explosive fuse placed in its shaft (see figure 2b). In these experiments, synchronization of the firing of the detonator with the mass spectrometer recording was achieved and chosen delay times were possible.

b) Laser-induced Decomposition

Laser irradiation of a sample in the chamber was achieved by using the transparent windows. The Bradley ruby laser ($\lambda = 694.3$ nm) was first aligned with the help of a small He-Ne continuous laser which was mounted on the same optical bench. A lens was used to focus the ruby beam onto the crystal surface to an area of ca. 2.0 ± 0.5 mm in diameter. An ion-repeller grid operating at positive voltage was situated between the sample and the ion source. When operated in Q-switched mode, the ruby laser has a peak power of ca. 200 MW and a pulse duration of ca. 20 ns. In the decomposition experiments, energy inputs into the crystals were in the range of 0.1 to 1 J. The valve leading to a Ferranti ion pump was adjusted such that the pressure inside the system did not exceed 10^{-5} torr at maximum gas evolution.

c) Laser Initiation

In a separate series of experiments, the conditions for the laser initiation of PETN in the vacuum system were investigated. Various experimental arrangements were used. In experiments with solid PETN, single crystals with their back surface coated with a thin film (ca. 100 nm) of aluminium were used. The crystals, of millimeter dimensions, were either mounted freely (unconfined) on a support, or embedded in epoxy resin to study the effect of confinement. Molten PETN was obtained using the arrangement illustrated in figure 3. The aluminium block was in contact with a hot plate. When the temperature was raised above the melting point (414 K), the melt was trapped between the microscope slide and the aluminium block. In an alternative apparatus a molten layer was produced without the confining glass slide.

4 RESULTS

a) Fracture-induced Decomposition

The fracture of a PETN crystal by an explosively driven chisel created new surfaces together with the rapid evolution of gases. The fracture

surfaces for this energetic mode of fracture were invariably rough (figure 8b). Their mass spectra showed distinct features different from that of thermal decomposition. In the low mass region, peaks at m/e 16(O), 28(CO), 30(NO), 44(CO₂,N₂O) were produced. However, no peak at m/e 46(NO₂) was observed. In the high mass regions, the only prominent peak was at m/e 60. Figure 4 is a step-wise presentation of the mass spectra taken 700μs after the firing of the detonator. The entire mass spectra of the reaction products are given in figure 5 which was taken with a time delay of 350 μs.

In contrast, the low energy fracture mode, achieved by the method of figure 2a, produced a number of different spectra which depended on the amount of energy transmitted to the crack. Three types of spectra were observed.

i) a large intense peak at m/e 76 plus other weak ones. An example is shown in figure 6.

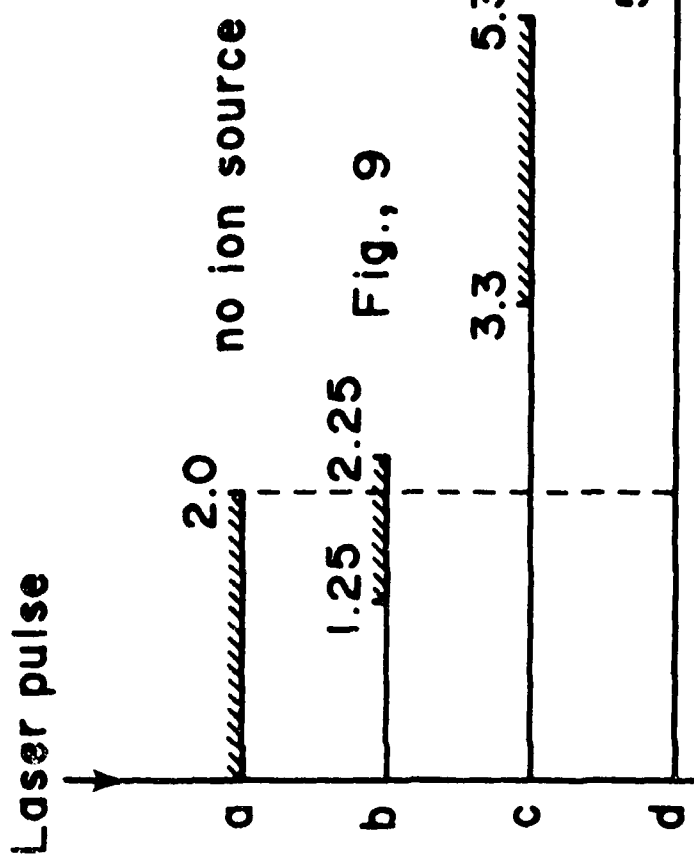
ii) a large intense peak at m/e 60 plus others. This type is similar to the example given in figure 4.

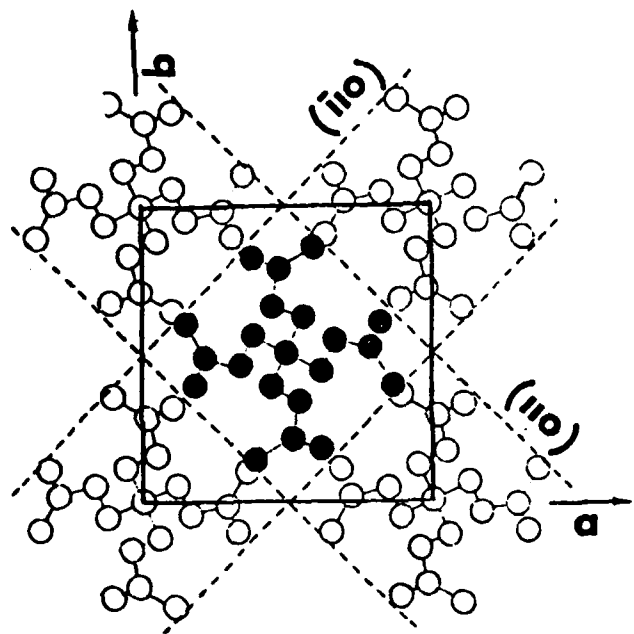
iii) the simultaneous presence of both peaks at m/e 76 and 60 in addition to others. An example is illustrated in figure 7.

The presence of a peak at m/e 76 is also accompanied by a peak at m/e 46 in the low mass region. The observed fracture surfaces were smooth (figure 8a gives an example) for spectra (i), rough for spectra (ii) and partly smooth and partly rough for spectra (iii). The smooth surfaces were (110) cleavage faces and were obtained when the chisel was accurately aligned and the minimum of energy used.

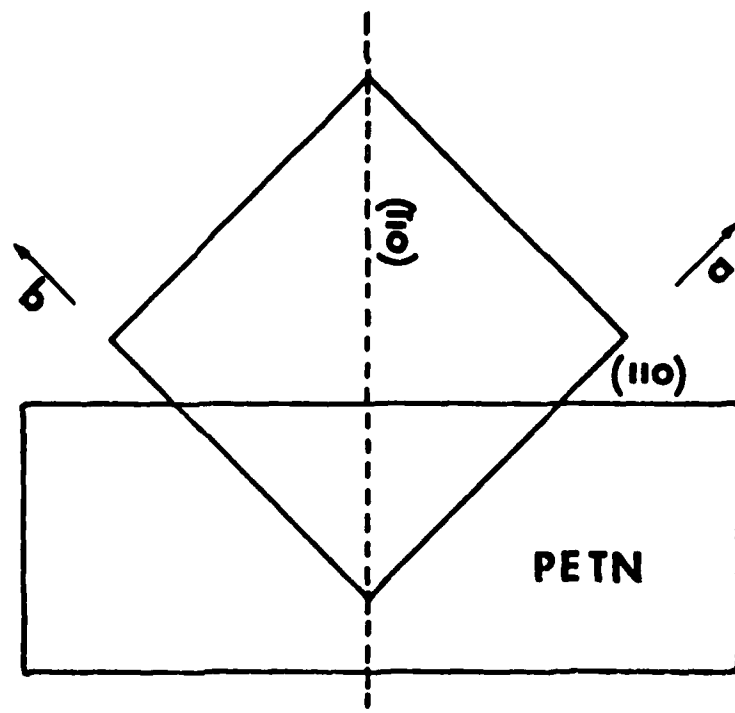
b) Laser-induced Decomposition

The interaction of a Q-switched ruby laser pulse with a PETN crystal inside the UHV system produced positively charged species which were detected for a duration of ca. 2 ms after the firing of the laser pulse even without the ion-source of the spectrometer in operation. A repeller

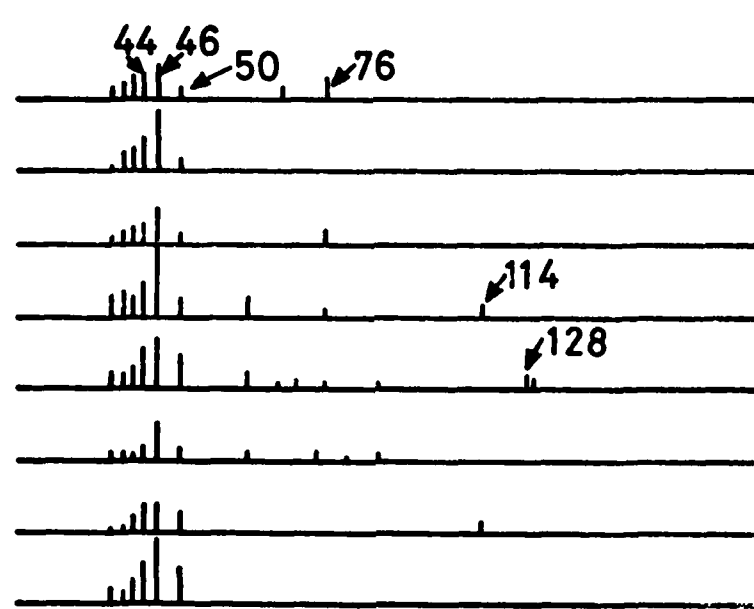




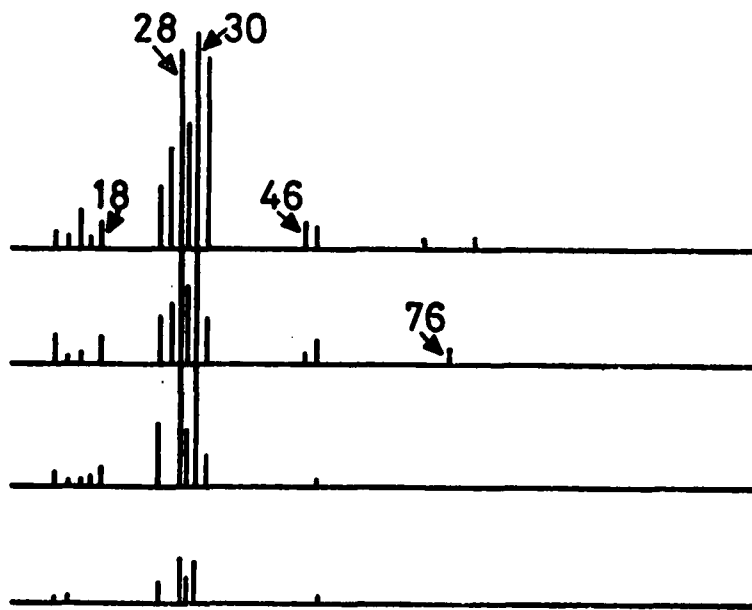
12



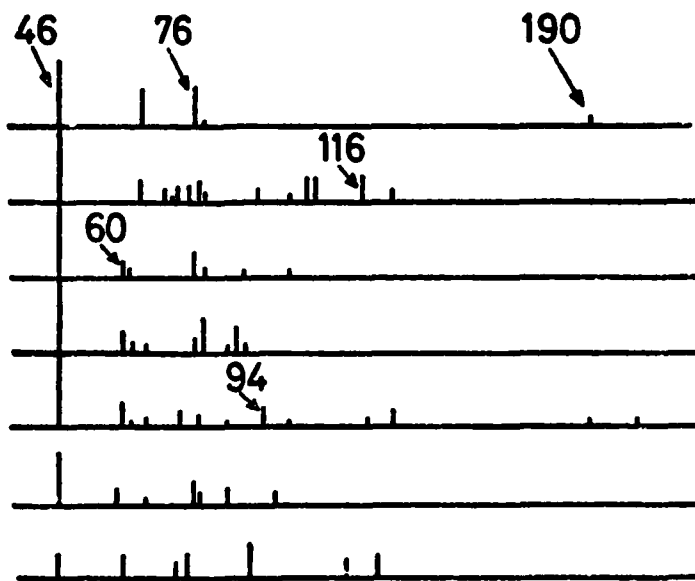
13



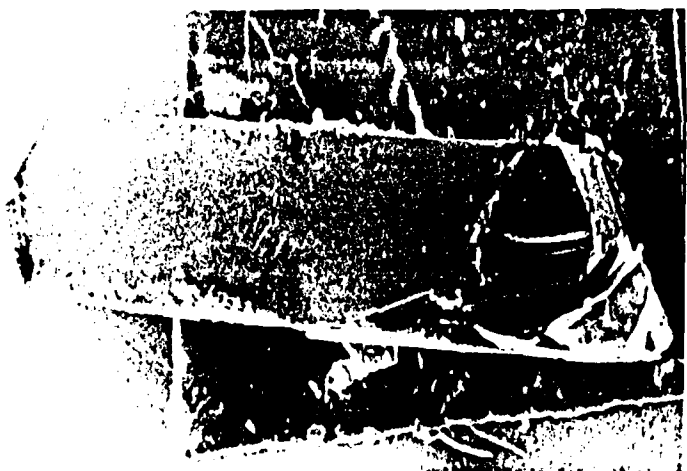
11



9



10



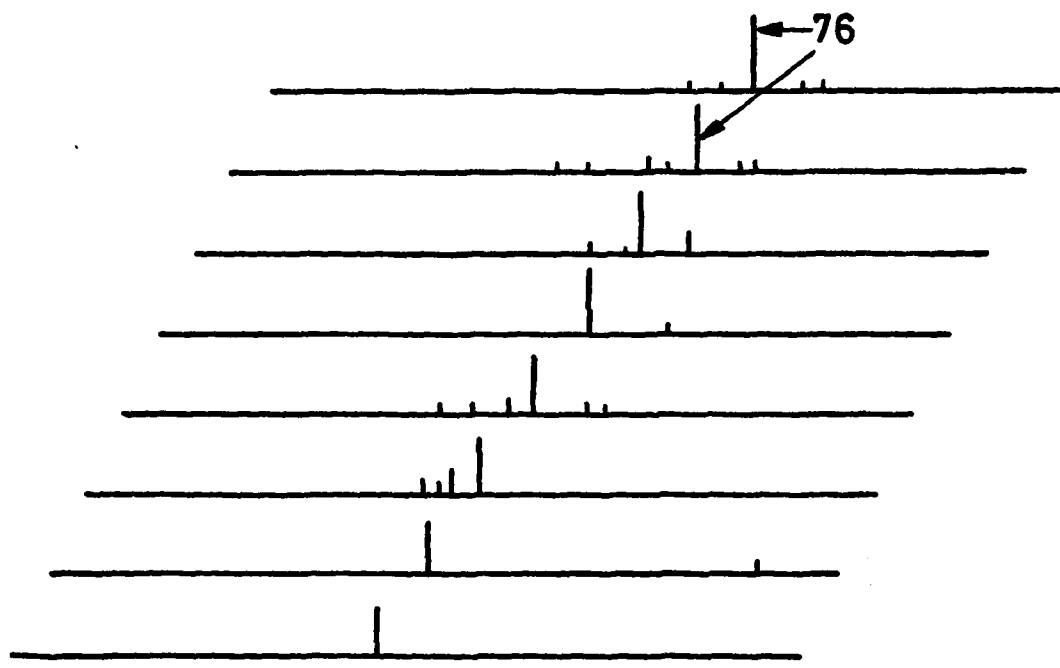
8a

1mm

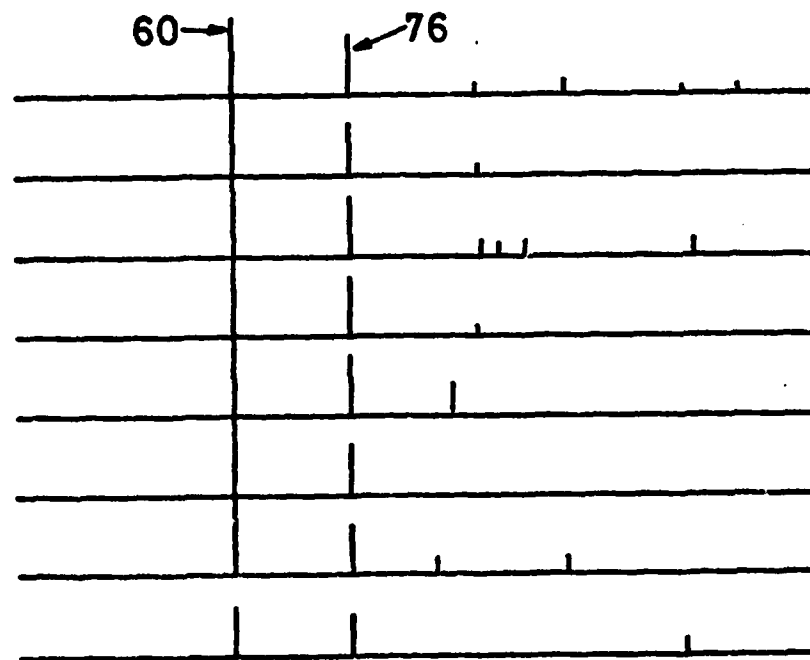


8b

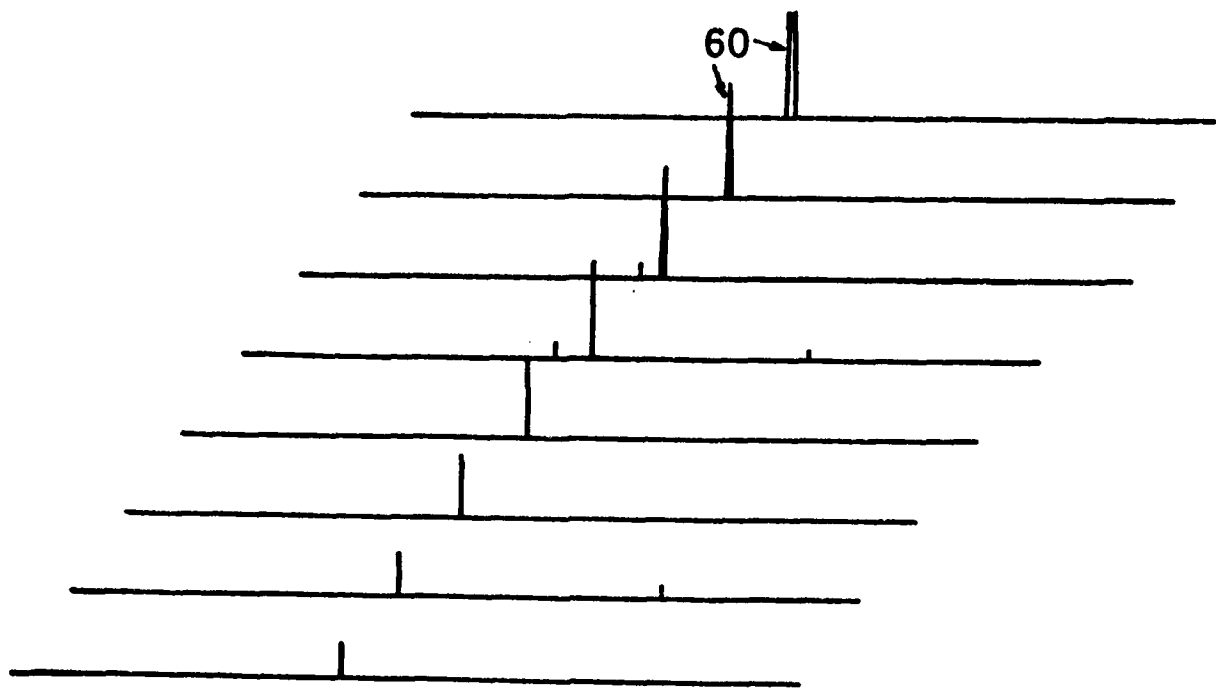
1mm



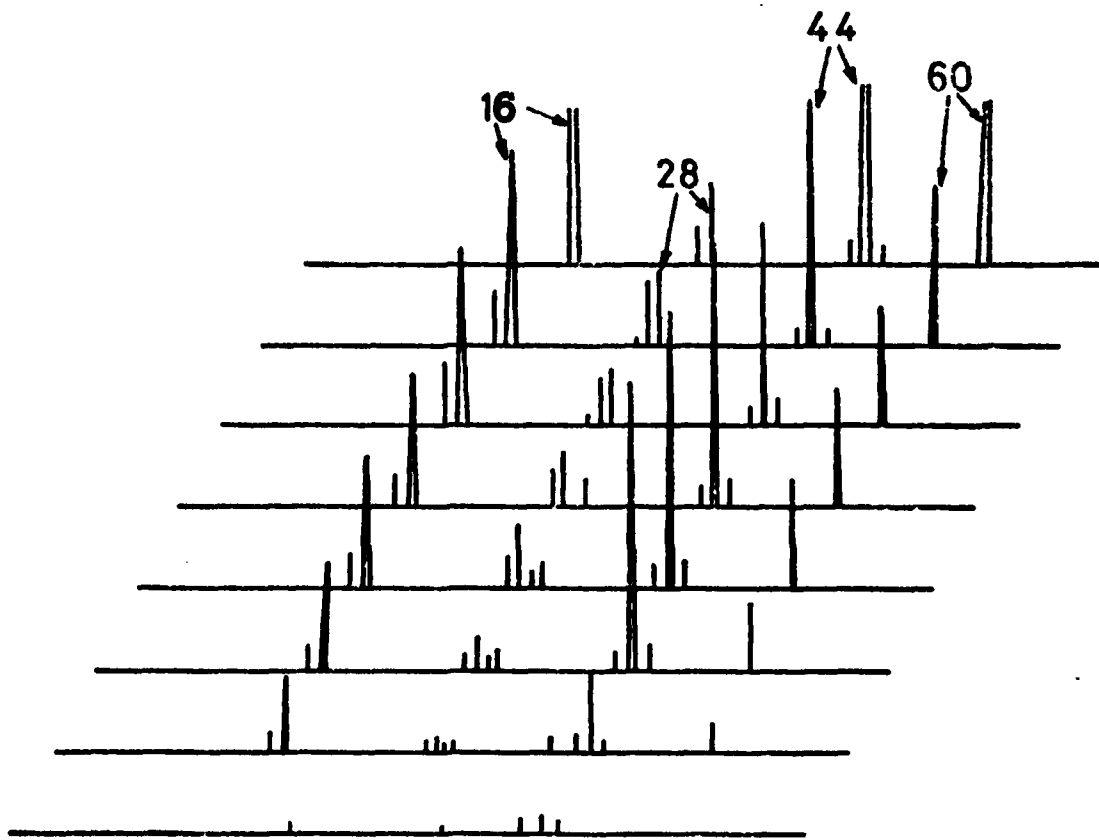
6



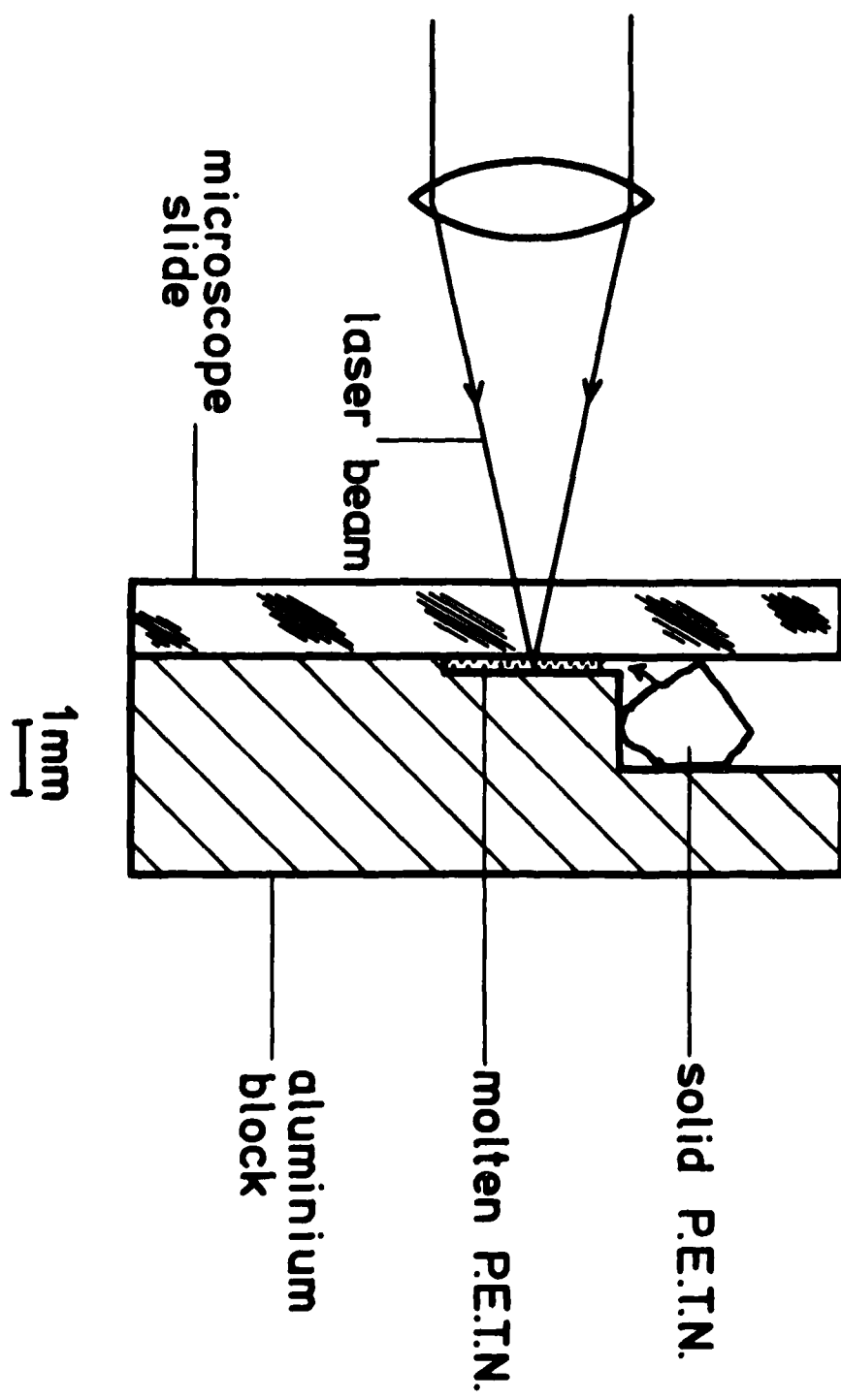
7



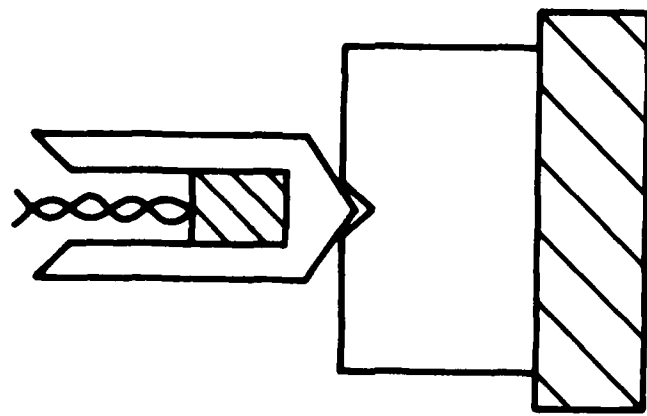
4



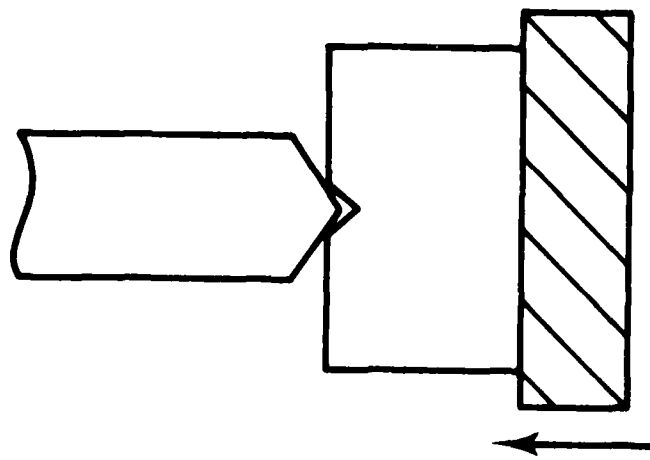
5

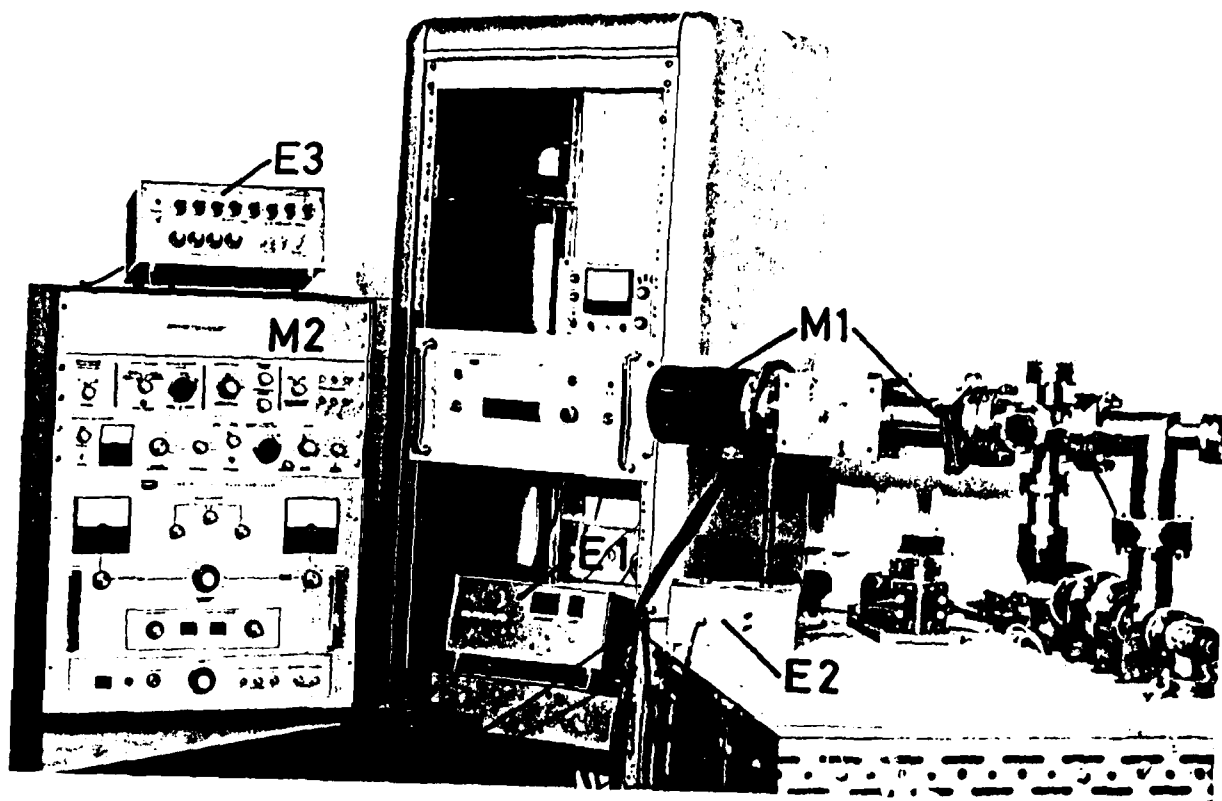


(b)



(a)





1

$$\frac{1}{2} - x, y + \frac{1}{2}, \frac{1}{2} - z; x + \frac{1}{2}, \frac{1}{2} - y, \frac{1}{2} - z; y + \frac{1}{2}, x + \frac{1}{2}, z + \frac{1}{2};$$

$$\frac{1}{2} - y, \frac{1}{2} - x, z + \frac{1}{2}$$

The tetragonal unit cell which contains two molecules of PETN is depicted in figure 12 which shows projection onto the (001) plane. The cleavage planes are (110) and ($\bar{1}\bar{1}0$) since only the weak van der Waals forces need to be overcome along these planes. Figure 13 shows the position of the cleavage plane (110) relative to another cleavage plane (110) which is also one of the surfaces of the as-grown crystal. However, the rapid fracture, initiated by the explosively-driven chisel, does not remain on the planes but penetrates and bifurcates into many non-cleavage planes thus producing a rough conchoidal surface (figure 8b). As the crack propagates along the terrain of this rough surface, it has to overcome and break off all chemical bonds that are transverse to its path. However, if fracture is confined along the cleavage plane, then no such rupture of chemical bonds takes place. The fractured surfaces are then smooth as illustrated in figure 8a. In this latter event the energy at the crack tip dissipates in the form of heat causing those molecules at the tip to sublime and subsequently decompose in the vapour phase. The mass spectrum is similar to the one obtained from thermal decomposition in which a PETN molecule decomposes via a molecular elimination mechanism (Ng et al 1976). The prominent peak in the high mass region at m/e 76 is attributed to the species $\text{CH}_2\text{ONO}_2^+$ derived from the parent molecule CH_3ONO_2 . The distinct difference in the mass spectrum of the decomposition products and its correlation with the mode of fracturing strongly suggest that there are two different decomposition pathways for the fracture-induced decomposition of PETN. Indeed both the reaction pathways can occur simultaneously if fracture occurs partly along the cleavage plane and partly by bifurcating into many non-cleavage planes. In such cases the mass spectrum shows the presence of both the peaks at m/e 60 and m/e 76 (see figure 7) in the high mass region.

cleavage at the four central C - C bonds and that the fragments $\cdot\text{CH}_2\text{ONO}_2$ and $\cdot\text{C}(\text{CH}_2\text{ONO}_2)_2$ rapidly degrade to CO and NO.

In the mass spectrometer, the species $\text{CH}_2\text{ONO}_2^+$. if present, should appear at m/e 76. The fact that it is absent in our TOF mass spectra for energetic fracture indicates that this radical is a short-lived species with a life-time less than the time resolution, 33 μs , of the spectrometer. There are two degradation pathways for this radical

- i) $\cdot\text{CH}_2\text{ONO}_2 \rightarrow \cdot\text{CH}_2\text{O} + \text{NO}_2$
- ii) $\cdot\text{CH}_2\text{ONO}_2 \rightarrow \cdot\text{CH}_2\text{ONO} + \text{O}$

The absence of a peak at m/e 46 (NO_2^+) rules out pathway (i). The presence of a peak at m/e 60 ($\cdot\text{CH}_2\text{ONO}^+$) and m/e 30 (NO^+) (which reflects easy cleavage of the alkyl nitrite at RO-NO) supports pathway (ii).

The bond dissociation energy for a typical $(\text{CH}_3)_3\text{C}-\text{CH}_3$ molecule is 290 kJ mol⁻¹ (Benson and O'Neal 1970) and for RO-NO₂ is 173 kJ mol⁻¹ (Levy 1954, 1956). When some of the elastic strain energy dissipated at the crack tip goes into promoting chemical decomposition, the molecule should decompose via the rupture of the weaker bond. Our result showed that it is the stronger C-C bond that is broken whereas the weaker RO-NO₂ bond remains intact. This implies that the energy associated with the crack tip is localised specifically on the C-C bond and that this bond is traversed by the crack in a time comparable to that required for one vibration. For this reason there is no possibility for the molecule to attain thermal equilibrium.

PETN crystallises from acetone in a tetragonal crystal system with space group P4₂1c (Wyckoff 1960). The molecule which has S₄ symmetry has four identical CH_2ONO_2 groups attached to the central carbon which occupies special positions, 0, 0, 0 and 1/2, 1/2, 1/2. The other carbon atoms are situated at the general positions x, y, z; \bar{x} , \bar{y} , \bar{z} ; \bar{y} , x, \bar{z} ; y, \bar{x} , \bar{z} ;

Unconfined crystals simply lost the aluminium film during laser irradiation and showed only a small crater formed at the focal point. Crystals confined in epoxy resin, were shattered into small pieces and it is probable that initiation could have been achieved with a slightly higher laser energy.

5 DISCUSSION

a) Fracture-induced Decomposition

When a fast moving crack propagates through a solid, the condition for crack growth in terms of a Griffith-type energy balance is given by (Bowden, Fox and Soria-Ruiz 1968, Fox and Soria-Ruiz 1970):

$$d\{E_E - [E_S + E_K + E_P + E_C]\}/dc \geq 0$$

where c is the crack length and the subscripts for the energy (E) terms represent the contribution of elastic, surface, kinetic, plastic and chemical energies respectively. Fracture studies on PETN crystal (Hagan and Chaudhri 1977) have shown that it is a weak solid which undergoes brittle fracture with limited plastic flow. Its fracture surface energy of 0.11 J m^{-2} is typical of that for a van der Waals solid. A characteristic of brittle fracture is that cracks can reach very high velocities of the order of a thousand metres per second depending on the solid (see, for example, Field 1970 for a review). The crack tip radius is of the order of atomic dimensions, and when it develops it does so by a process of breaking atomic bonds. In their work on fracture-induced decomposition in brittle crystalline solids Bowden, Fox and Soria-Ruiz reported the evolution of single gaseous species from metal carbonates and azides as a result of fracturing these solids. However in the more complex PETN crystal there is more than one type of chemical bonding present in the molecule. Their preliminary results suggested that decomposition takes place via the

voltage of 3 V was needed to stop these charged species from entering into the ion source to observe the mass spectra of the decomposition products.

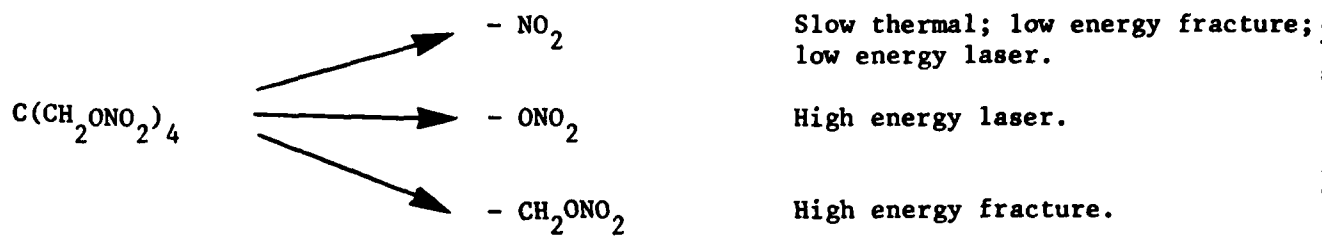
With the ion repeller set at 3 V DC, the ionisation potential at 70 eV and the time delay at 1.25 ms the mass spectrum (shown in figure 9) revealed the presence of decomposition products similar to that obtained from our thermal decomposition work. With a longer time delay of 3.3 ms, more peaks (*m/e*, 60, 62, 65, 71, 74, 76, 94, 114, 116, 128, 190, etc) were observed in the high mass region (figure 10). All of these were transient with the exception of *m/e* 76 which was particularly persistent. At a time delay of 5.6 ms many of those peaks were still present but with diminishing intensity whereas the peak at *m/e* 76 appears in every step (figure 11).

c) Laser Initiation

The results of the laser initiation experiments are summarised in table 1. Only under one set of conditions (PETN in liquid phase, confined and irradiation by a Q-switched laser pulse) could initiation of PETN by ruby laser irradiation in vacuum be effected for the energies used. Solid PETN could not be initiated by laser irradiation under vacuum conditions for the range of energies available.

TABLE 1
Laser initiation of PETN in vacuum

<u>PETN phase</u>	<u>Confinement</u>	<u>Laser pulse</u>	<u>Explosion</u>
Solid	Yes	Non Q-switched (20 J)	No
Solid	Yes	Q-switched (1 J)	No
Solid	No	Non Q-switched (20 J)	No
Solid	No	Q-switched (1 J)	No
Liquid	No	Non Q-switched (20 J)	No
Liquid	No	Q-switched (1 J)	No
Liquid	Yes	Non Q-switched (20 J)	No
Liquid	Yes	Q-switched (1 J)	Yes



15

5. **The deformation stress of highly brittle explosive crystals from real contact area measurements**

M. MUNAWAR CHAUDHRI
Cavendish Laboratory, Madingley Road, Cambridge, UK

An experimental study is described in which the deformation stress of millimetre-size highly brittle as-grown single crystals of explosive materials has been determined using a novel experimental technique. The technique involves the loading of the test crystal against a transparent glass plate with *in situ* measurements of the real area of contact under load using an optical microscope. For all explosive crystals the deformation stress was found to increase with load reaching a plateau at higher loads. The maximum deformation stress of a crystal was found to be considerably lower than its Vickers diamond hardness value. A discussion on the determination of the uniaxial yield stress of small particles is also given.

1. Introduction

Recently, Chaudhri [1] published a model for the initiation of explosions in compacts of sensitive solid explosives when they are impacted by hard needle-shaped strikers. According to this model, an explosion results due to the high temperatures generated by friction at the contacting surfaces of the explosive particles which are picked up by the striker's tip and carried into the explosive compact. To make reliable quantitative estimates of the temperatures generated at the rubbing surfaces, a knowledge of several physical properties of the particles is needed [1]. One such property of significant importance is the deformation stress of a particle pressed against another with a given normal load. To determine this parameter direct measurements of the real area of contact are required, which are difficult to make even for ductile metals as has recently been pointed out by Tabor [2]. For brittle materials the situation is further complicated by cracking which can occur at quite small loads. Here the results of a novel experimental investigation are reported in which the deformation stress of a number of highly brittle [3, 4] as-grown explosive crystals has been determined from measurements of the real area of contact when they are pressed against

a hard transparent surface with a known normal load. In the literature, such a method of determining the deformation stress of brittle crystals of shapes other than the rectangular parallelopiped does not appear to have been reported before.

2. Experimental details

2.1. Materials

Single crystals of lead azotetrazole (LAT) of types A and C were obtained from Dr P. Collins of PERME (UK); type A were of pyramidal shape about 2 mm across, whereas type C were needle-like 1 to 2 mm in length and about 0.5 mm in diameter. Single crystals of α -lead azide were grown in the laboratory by a diffusion method [5]; these were also needle shaped, 0.3 to 0.5 mm in diameter, and 1 to 2 mm in length. Crystals of β -cyclotetramethyl-tetranitramine (β -HMX) and cyclotrimethylenetrinitramine (RDX) were also grown in the laboratory by slow evaporation of a saturated solution in acetone at 70°C. β -HMX single crystals were thick platelets with relatively good edges, whereas crystals of RDX did not show sharp edges and generally had rounded corners. Potassium chloride crystals about 1 cm \times 1 cm \times 1 cm in size were obtained from BDH (UK), from which pieces about 1 to 2 mm in size were cleaved for these

TABLE I Chemical formulae and some crystallographic and mechanical properties of the crystals used in this work

Material	Chemical formula	Crystal class and space group	Primary glide system
α -lead azide (α -PbN ₃)	PbN ₃	Orthorhombic Pcmn [6]	not known
Lead azotetrazole (LAT) type A	[C _x N ₁₀ Pb] _x · H ₂ O (x between 0 and 2)	not known	not known
type C	[C _x N ₁₀ Pb] · Pb(OH) ₂	not known*	not known
β -cyclotetramethylene- tetranitramine (β -HMX)	(CH ₂ NNO ₂) ₄	monoclinic P2 ₁ /C [8]	not known
Cyclotrimethylene- trinitramine (RDX)	C ₃ H ₆ N ₃ (NO ₂) ₃	orthorhombic Pbca [9]	(010){001} (10)
Potassium chloride (KCl)	KCl	cubic Fm 3F [11]	{110}{110} (12)

*Melanie A. Pierce-Butler [7] has determined the structure of LAT type D having the same chemical formula as that of the type C; the crystal class is triclinic and space group P1.

experiments. Table I lists the chemical formulae of the various explosives along with their crystal structures and slip systems (if known).

2.2. The principle of the experimental technique

The principle of the technique can be illustrated with the help of Fig. 1. In Fig. 1a a light beam is reflected from a partially silvered surface S and hits a polished glass plate normally. If the refractive indices of the glass and air are n_1 and n_2 respectively, then the intensity I_1 of the light reflected from surface A, for unit incident intensity, is:

$$I_1 = \left(\frac{n_1 - n_2}{n_1 + n_2} \right)^2 \quad (1)$$

Substituting $n_1 = 1.5$, and $n_2 = 1$, we have $I_1 = 0.04$.

A crystal of the test material is then brought

into perfect contact at surface A as shown in Fig. 1b. The intensity I_2 of the light reflected from the glass/crystal interface is then given by:

$$I_2 = \left(\frac{n_3 - n_1}{n_3 + n_1} \right)^2 \quad (2)$$

where n_3 is the refractive index of the crystal. For the crystals used in this work n_3 is in the range 1.5 to 2.6. Taking a value of n_3 of 1.6 (say), $I_2 = 0.0066$, which is considerably smaller than I_1 . The same is true for other values of n_3 in the given range. Thus, the reduction in the intensity of the reflected light gives us a convenient method of measuring the area of real contact between a non-metallic crystal and a transparent glass plate.

2.3. The compression apparatus

A schematic diagram of the arrangement used for compressing crystals against an optically flat glass surface and simultaneously measuring the area of

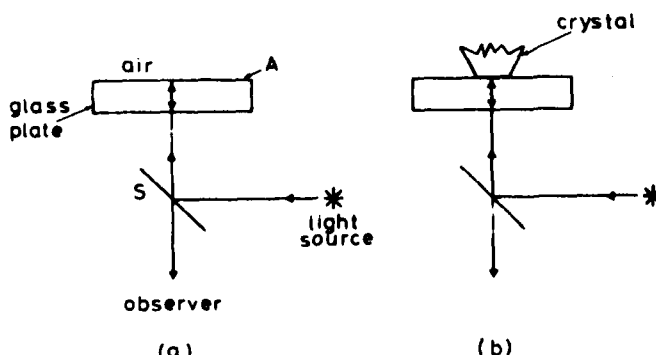


Figure 1 Diagram showing the principle of the experimental technique used for measuring the real area of contact.

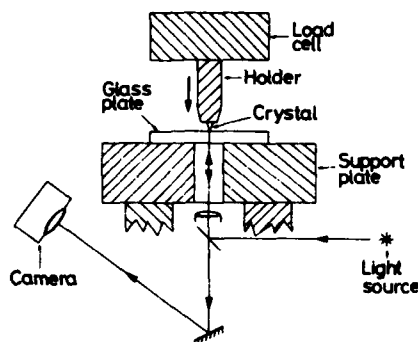


Figure 2 Schematic diagram of the arrangement used for measuring the real area of contact of a crystal loaded against a smooth glass plate.

real contact between the crystal and the glass surface is shown in Fig. 2. The crystal to be examined is mounted on a steel holder with an epoxy "araldite". Before the epoxy hardens, the crystal is carefully positioned so that as far as possible a sharp corner of the crystal is along the axis of the holder, or a sharp edge is normal to it.

The steel holder itself is screwed into a sensitive load cell capable of measuring loads from less than a gramme to several kilograms. The load cell is rigidly mounted on the crosshead of a mechanical testing machine (Instron No. 1122); in all experiments the crosshead speed was 0.05 mm min^{-1} . The glass plate is placed on a thick steel support plate and the contact area between the crystal and the glass plate is viewed in reflection using an optical microscope focused on the glass surface, as shown in the figure. When desired, photographs of the contact area are taken, the magnification on the camera film being $\times 60$.

The experimental procedure was as follows. First the crystal was brought to within 5 to $10 \mu\text{m}$ of the glass surface and a photograph taken. At this stage the field of view was uniformly illuminated. Then the crystal was brought into contact with the glass surface, with the normal load being a gramme or less. It was observed that wherever the crystal made real contact with the glass surface, the intensity of illumination decreased markedly. The load was then further increased by a small amount and another photograph taken. This procedure was continued for several loads and a corresponding sequence of photographs was made.

The maximum load applied on a crystal depended upon its size and the type so that only

a minimum amount of cracking occurred. Photographs were also taken during the unloading of the crystal and it was found that in all cases plastic deformation of the crystal had occurred over the entire region in real contact with the glass plate. The deformed region was flat and optically smooth and when the crystal was only just removed from the glass plate the flat gave a mirror-like reflection.

Silhouette optical micrographs of crystals before and after deformation were also taken. Although the deformed regions were relatively small, in some cases the deformation could be clearly seen in the micrographs.

The measurements of the real area of contact were made from enlarged prints using a transparent millimetre grid. In this manner, a real contact area as small as $1 \mu\text{m} \times 1 \mu\text{m}$ could be measured.

3. Results

The results from different crystals are given below separately.

3.1. $\alpha\text{-PbN}_6$

Two single crystals of this material were investigated. Fig. 3a shows the profile of a crystal before it was deformed. It was loaded on an edge (marked with arrow) along the *c*-axis, and the photographs of real contact are shown in Fig. 3b. The load on the crystal in grammes is shown alongside each frame. In the uppermost frame, the crystal has not touched the glass plate and is only a few μm from the surface. Note that the entire field is uniformly illuminated (the black circular spot in the centre of frames 1 and 2 is due to a dust particle). In frame 2, the load has been increased to 10.5 g and a dark band has appeared in the centre. The crystal is in real contact with the glass surface at all points in the band. In the next frame, the load has been further increased to 20 g, and note that the area of the dark band has also increased. The crystal was then unloaded, first to 4 g and then to zero. At 4 g the area of the dark region in the band has decreased as some of it has become brighter than the background. At zero load, the entire band has changed into a bright one. These observations strongly indicate that the crystal is no longer in contact with the glass plate and that the edge of the crystal had plastically deformed to a smooth flat surface.

The crystal was then again loaded and the real areas of contact corresponding to loads of 24, 32 and 41 g are also shown in the figure. As the load

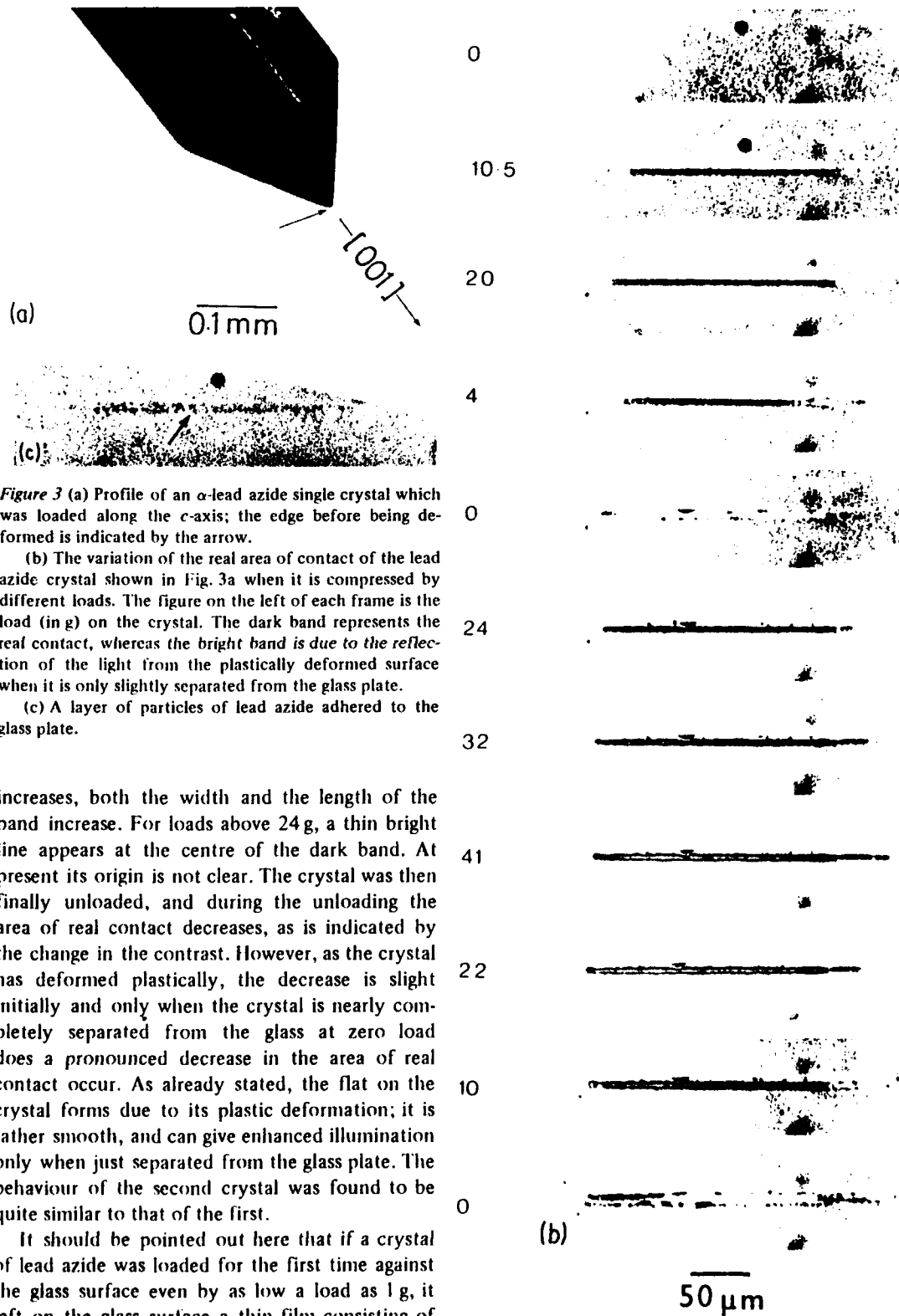


Figure 3 (a) Profile of an α -lead azide single crystal which was loaded along the c -axis; the edge before being deformed is indicated by the arrow.

(b) The variation of the real area of contact of the lead azide crystal shown in Fig. 3a when it is compressed by different loads. The figure on the left of each frame is the load (in g) on the crystal. The dark band represents the real contact, whereas the bright band is due to the reflection of the light from the plastically deformed surface when it is only slightly separated from the glass plate.

(c) A layer of particles of lead azide adhered to the glass plate.

increases, both the width and the length of the band increase. For loads above 24 g, a thin bright line appears at the centre of the dark band. At present its origin is not clear. The crystal was then finally unloaded, and during the unloading the area of real contact decreases, as is indicated by the change in the contrast. However, as the crystal has deformed plastically, the decrease is slight initially and only when the crystal is nearly completely separated from the glass at zero load does a pronounced decrease in the area of real contact occur. As already stated, the flat on the crystal forms due to its plastic deformation; it is rather smooth, and can give enhanced illumination only when just separated from the glass plate. The behaviour of the second crystal was found to be quite similar to that of the first.

It should be pointed out here that if a crystal of lead azide was loaded for the first time against the glass surface even by as low a load as 1 g, it left on the glass surface a thin film consisting of very small particles which could not be resolved

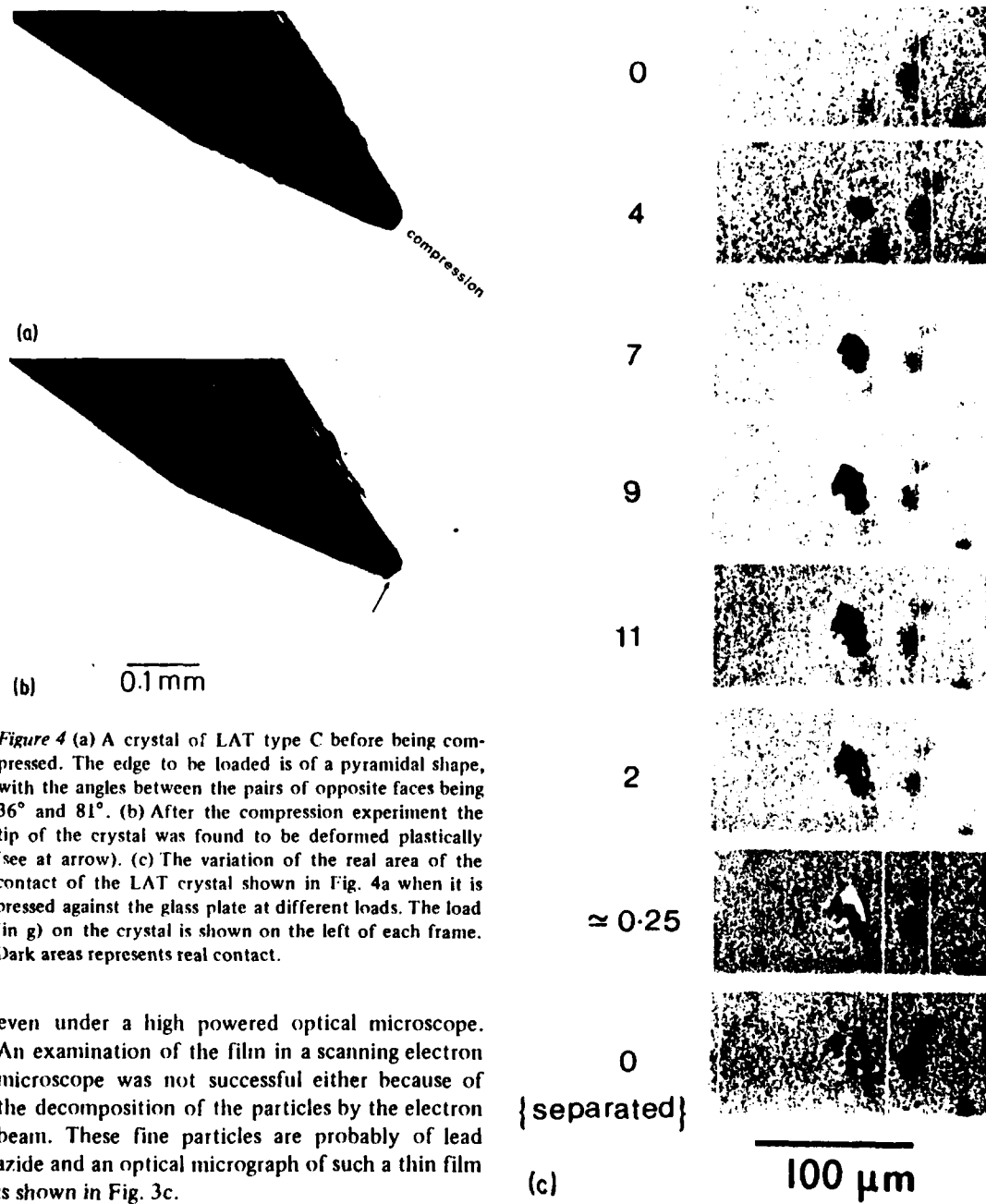


Figure 4 (a) A crystal of LAT type C before being compressed. The edge to be loaded is of a pyramidal shape, with the angles between the pairs of opposite faces being 36° and 81° . (b) After the compression experiment the tip of the crystal was found to be deformed plastically (see at arrow). (c) The variation of the real area of the contact of the LAT crystal shown in Fig. 4a when it is pressed against the glass plate at different loads. The load (in g) on the crystal is shown on the left of each frame. Dark areas represent real contact.

even under a high powered optical microscope. An examination of the film in a scanning electron microscope was not successful either because of the decomposition of the particles by the electron beam. These fine particles are probably of lead azide and an optical micrograph of such a thin film is shown in Fig. 3c.

Another interesting observation was that neither during the approach of a lead azide crystal towards the glass plate nor during the crystal's removal from the plate after having been loaded, were the surface or adhesive forces strong enough to be registered by the load cell. That is, these forces were less than 0.25 g.

3.2. LAT

We examined three crystals of LAT type "C" and

only one of LAT type "A". The compression behaviour of type "C" crystals was quite similar and results from a crystal are shown in Fig. 4c. The end of the crystal which was loaded was of pyramidal shape with the angles between the opposite faces being 36° and 81° . Figs. 4a and b show this end before and after deformation, respectively. The region which was loaded is indi-

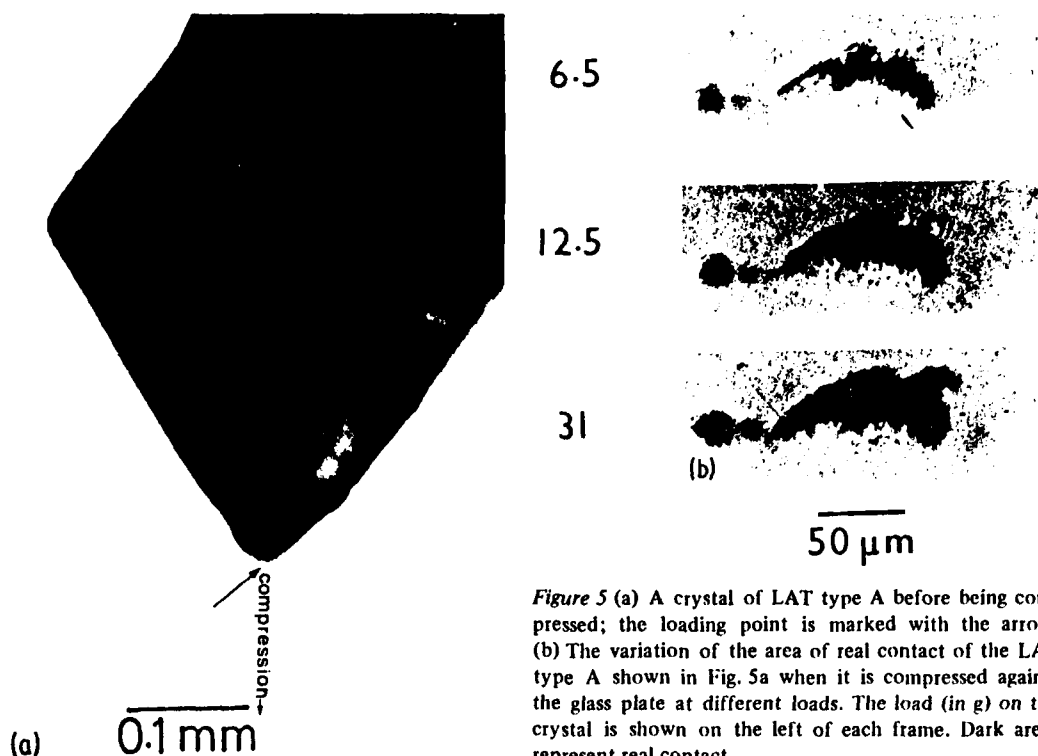


Figure 5 (a) A crystal of LAT type A before being compressed; the loading point is marked with the arrow. (b) The variation of the area of real contact of the LAT type A shown in Fig. 5a when it is compressed against the glass plate at different loads. The load (in g) on the crystal is shown on the left of each frame. Dark areas represent real contact.

cated with an arrow and it is quite clear that plastic deformation of the tip has taken place.

It will be seen from Fig. 4c that as the normal load on the crystal is increased from 0 to 11 g, the area of real contact also increases; in this case, because of the geometry of the loaded zone, the area of real contact is approximately circular. When unloading occurs and the load is reduced to 2 g, the area of real contact only reduces slightly, as in the case of lead azide. When the load is further reduced to 0.25 g, some separation of the surfaces occurs, as is evident from the very bright spot in the middle of the area of contact. When the surfaces are completely separated (i.e. last frame), there are still some dark areas left; these are due to an adhered layer of LAT on the glass surface.

Figs. 5a and b show a crystal of LAT (type A) before being compressed and the variation of real area of contact with load, respectively. As will be seen in Fig. 5a, the corner of the crystal which was loaded was not very sharp with the result that the contact occurs at several isolated areas (see Fig. 5b). Moreover, as for the above two materials, when the load was increased from 6.5 g to 31 g, the area of real contact also increased. On com-

plete unloading, a very thin layer of adhered particles (smaller than 1 μm) was left on the glass plate.

3.3. β -HMX

Two single crystals of this material were investigated, but photographs of the real area of contact of only one of them will be shown here. Fig. 6a shows the face of the crystal that was loaded (this crystal did not have any pronounced corners or sharp edges) and the variation of the area of real contact with load is shown in Fig. 6b; loads in grammes are given at the bottom left-hand corner of each frame. In this case, the real area of contact is not of a regular shape. Moreover, for loads greater than 21.5 g some fringes appear outside the area of real contact. Again, for these crystals the size of the area of real contact increased with load.

The plastic deformation of a sharp corner of the second crystal is clearly illustrated in Fig. 7. Fig. 7a shows the corner of the crystal which was loaded along the a -axis. Fig. 7b shows the state of the corner after the crystal had been loaded to 11 g and then unloaded. Note the permanent deformation of the corner, but no cracking is

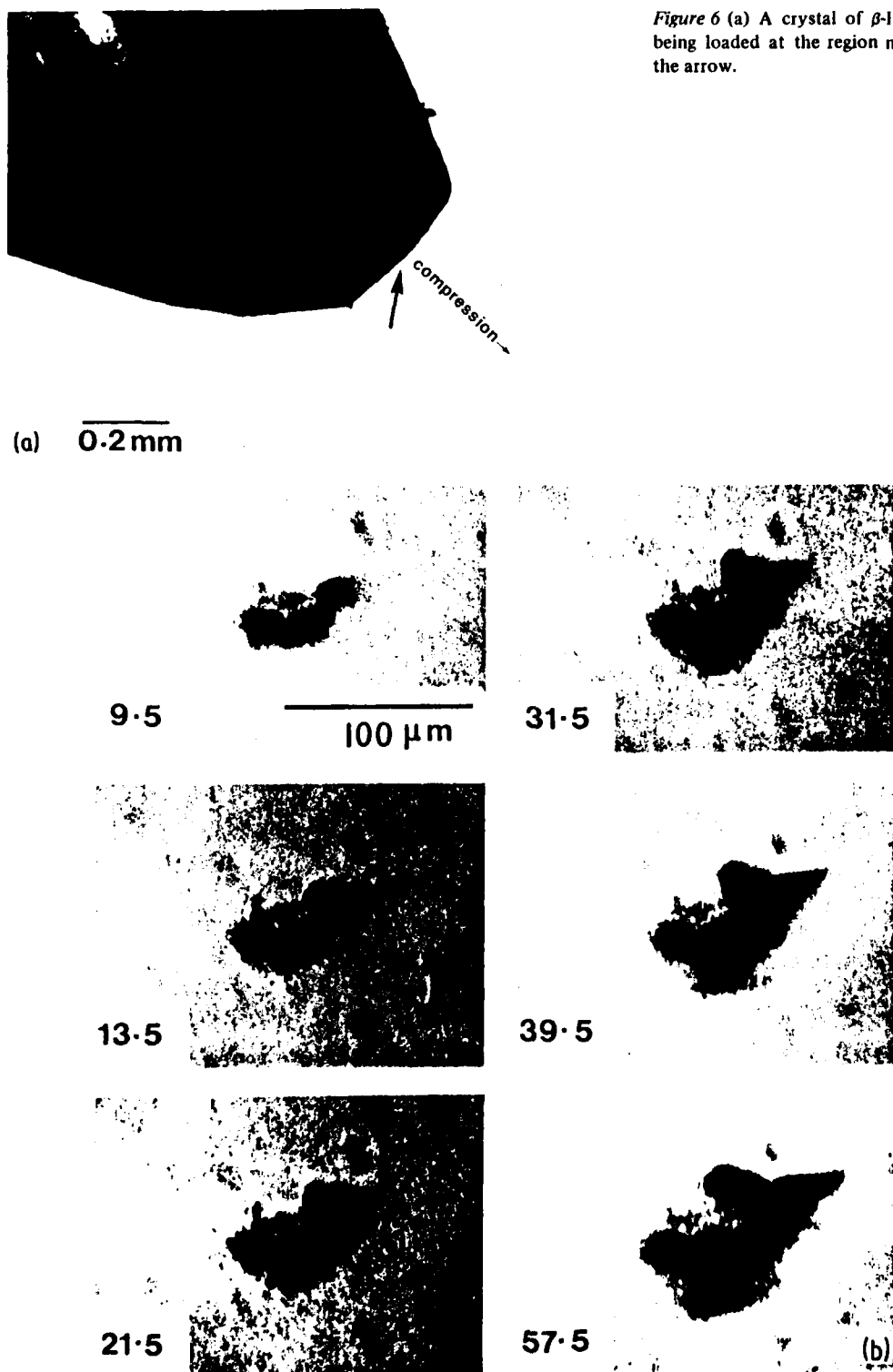


Figure 6 (a) A crystal of β -HMX before being loaded at the region marked with the arrow.

Figure 6 (b) The variation of the area of real contact of the β -HMX crystal shown in Fig. 6a when it is compressed against the glass plate at different loads. The load (in g) on the crystal is shown at the bottom left-hand corner of each frame. Dark areas represent the real contact. Note also the optical interference fringes for the three highest loads; these regions giving interference fringes are not in real contact.

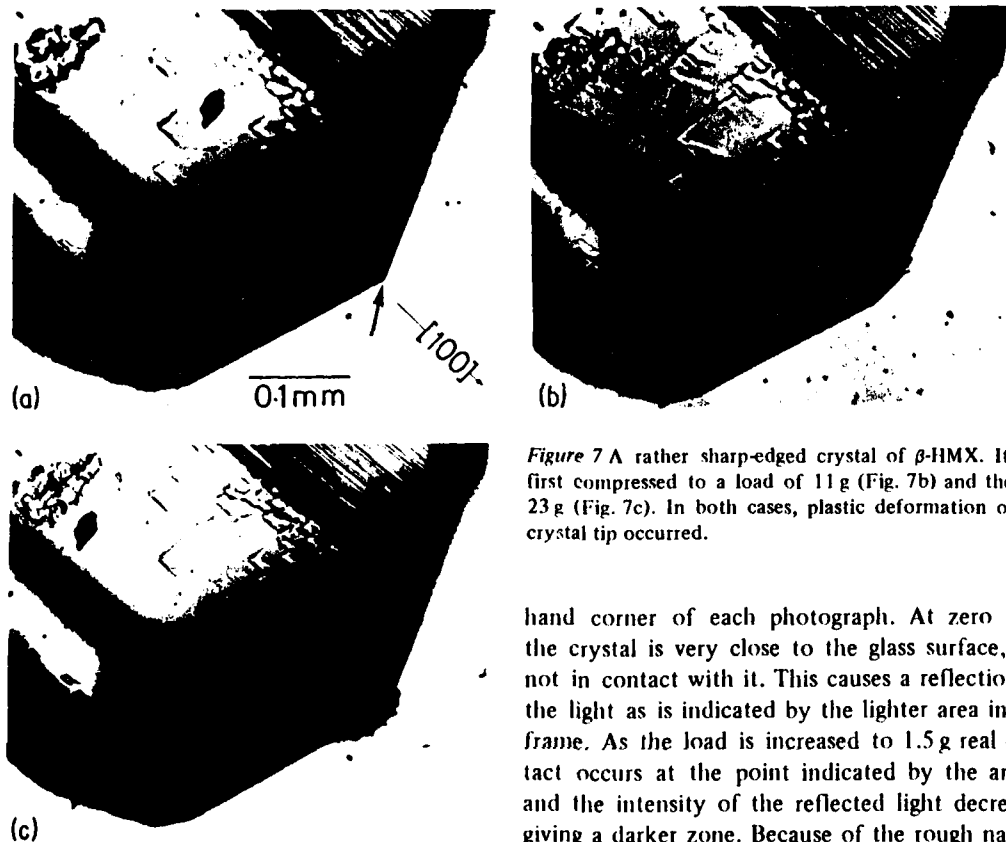


Figure 7 A rather sharp-edged crystal of β -HMX. It was first compressed to a load of 11 g (Fig. 7b) and then to 23 g (Fig. 7c). In both cases, plastic deformation of the crystal tip occurred.

hand corner of each photograph. At zero load the crystal is very close to the glass surface, but not in contact with it. This causes a reflection of the light as is indicated by the lighter area in the frame. As the load is increased to 1.5 g real contact occurs at the point indicated by the arrow and the intensity of the reflected light decreases giving a darker zone. Because of the rough nature of the crystal surface the contact occurs at several isolated zones as is clearly indicated by frames corresponding to higher loads. This sequence gives a clear example of the asperity contact described by Bowden and Tabor [13]. The maximum load applied to the crystal was 50 g (the corresponding

apparent yet. When the crystal was further loaded to 23 g and then unloaded, the volume in which permanent deformation occurred also increased (see Fig. 7c). This frame also indicates that some fracturing of the tip may have occurred. However, it cannot be said with any certainty whether the adhesion of the crystal tip to the glass enhanced the fracture.

It may be added here that a film of adhered fine particles of β -HMX crystals was left on the glass surface even after loading to only 3 g. Whether this film formed at lower loads was not examined.

3.4. RDX

Single crystals of this material were approximately spherical and of diameter less than 1 mm. Two crystals were investigated, but photographs of the area of real contact of only one of them will be shown here. In Fig. 8a the profile of a crystal is shown with an arrow marking the region which was loaded. Fig. 8c shows the variation of the size of the area of real contact with increasing load; the load in grammes is shown at the bottom left-

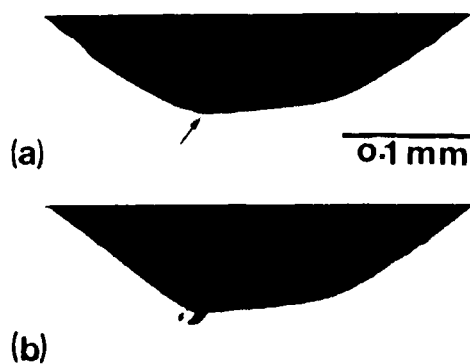


Figure 8 (a) Part of an RDX crystal which did not exhibit any sharp edges. It was loaded at the region marked with the arrow. (b) After loading to 41 g, a thin sliver of the crystal appears to be on the point of detaching when the crystal was separated from the glass plate.

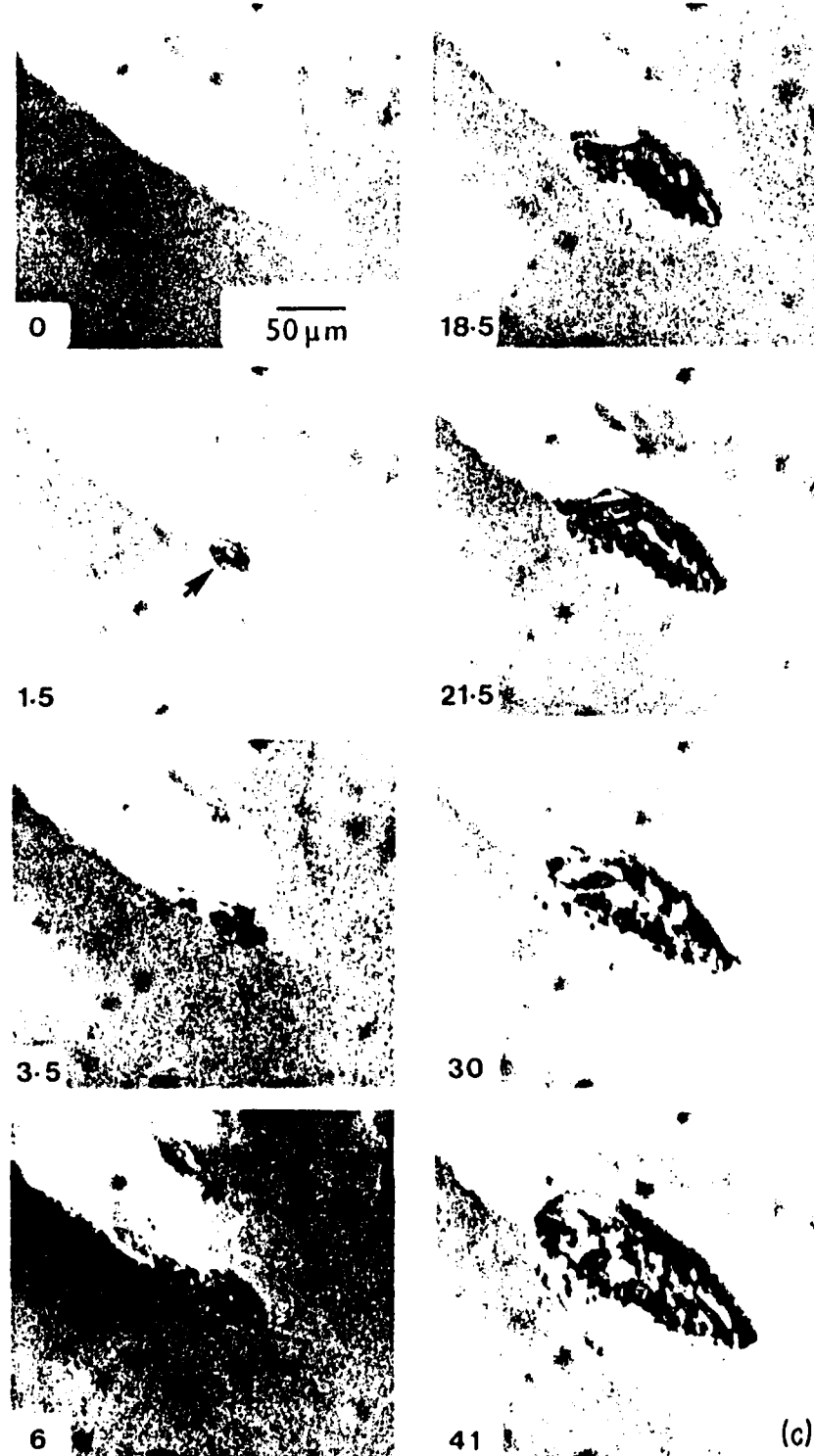


Figure 8 (c) The variation of the area of real contact of the RDX crystal shown in Fig. 8a when it is pressed against the glass plate at different loads. The load (in g) on the crystal is shown at the bottom left-hand corner of each frame. Dark areas represent the real contact.

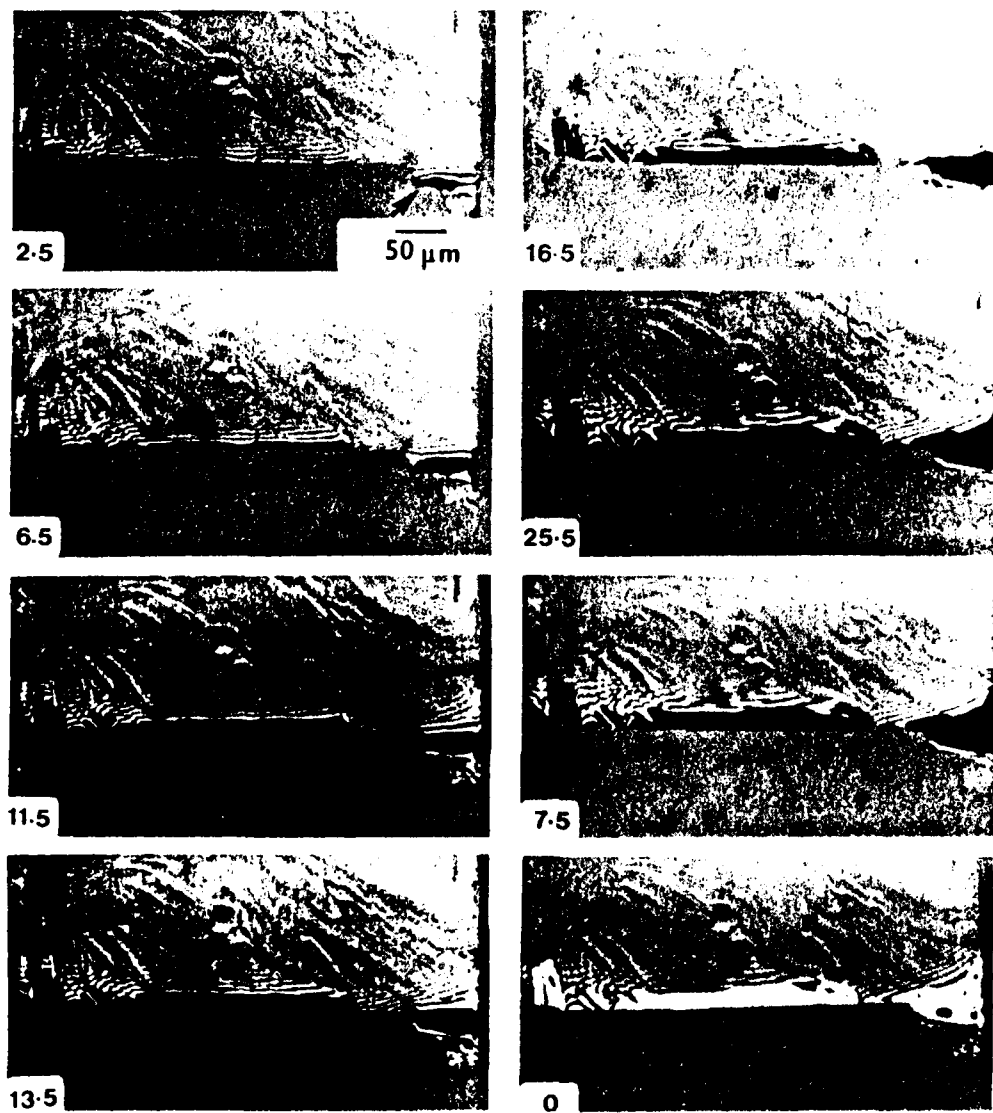


Figure 9 The variation of the area of real contact of a wedge-like crystal of KCl when it was compressed along [110] against the glass surface at different loads. The load (in g) is shown at the bottom left-hand corner of each frame. Dark areas represent the real contact. Note also the interference fringes; these correspond to regions outside the real contact.

area of real contact is not shown here) and then it was unloaded and again a very thin layer of extremely small particles was left adhering to the glass plate. A photograph of the crystal after the deformation is shown in Fig. 8b. It appears that a thin sliver of the crystal was in the process of being torn off at the contact zone.

3.5. KCl

Fig. 9 shows the variation of the real area of contact for a single crystal of KCl loaded on a fresh

edge formed by cleaving along {100} planes; the direction of compression was approximately along [110]. (Note that it is because of the lighting conditions that in the figure only one of the {100} faces forming the edge is seen.) In the first frame, the load is 2.5 g and real contact occurs at isolated points marked by the arrows; interference fringes are also clearly visible outside the real contact zone. As the load is increased, the number of zones in real contact and their areas increase, but no cracking of the crystal occurs. The load was

increased to 25.5 g and then the crystal was unloaded. Note that until the load has dropped to zero there is no significant reduction in the area of real contact (see the frame corresponding to 7.5 g). This strongly suggests that real area of contact is formed by plastically deformed area of the material. Naturally, as the load is decreased, the area of the plastically deformed flat will not reduce. When the load is reduced to zero and the surfaces are just separated, the plastically flowed material gives enhanced illumination. In the last frame (i.e. zero load) a very small zone is still in contact (dark zone marked with arrow); this dark zone also changed to a bright one on further separation. For this crystal no layer of transferred material was left on the glass plate.

4. Data reduction

The average contact stress was obtained by dividing the applied load by the corresponding measured area of real contact. As in all cases, even at the smallest loads studied, plastic deformation of the material had occurred over the entire contact zone, the average contact stress gives us the plastic deformation stress of the material. The variation of the deformation stress with load of the different crystals are shown in Figs. 10 to 14. Except for KCl, all crystals studied show that the deformation stress increases with load, reaching a plateau at higher loads. For crystals of different materials the average deformation stress at high loads was greater by a factor in the range 1.5 to 5.0 than that at low loads. Notice, however, that

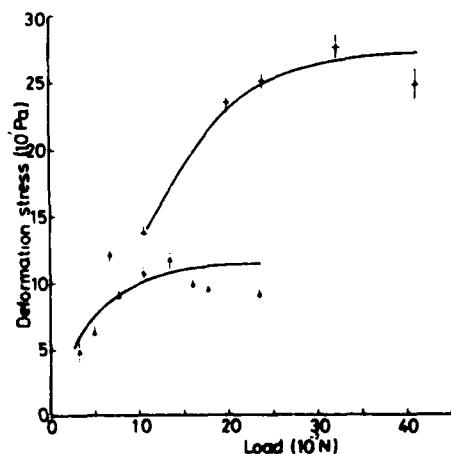


Figure 10 The variation of the deformation stress of α -lead azide crystals with load. •, crystal No. 1; ▲, crystal No. 2.

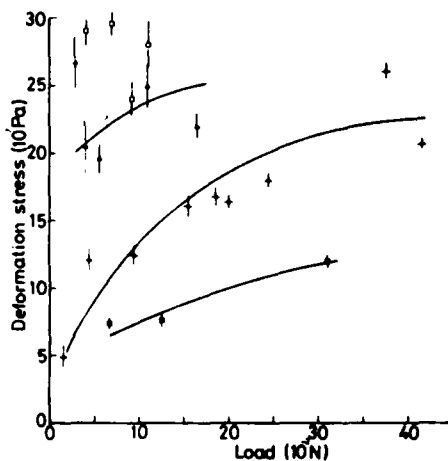


Figure 11 The variation of the deformation stress of LAT type C and type A single crystals with load. •, ▲, △, LAT type C crystal Nos. 1, 2 and 3 respectively; ■, LAT type A single crystal.

deformation stress against load graphs show irreproducible behaviour even for crystals of the same material. Several factors may contribute towards this irreproducibility: (i) a change of the loading axis of the crystal; (ii) a change in the geometry of the loaded region; and (iii) changes in the physical properties from crystal to crystal due to the impurity content variations.

For the case of α -lead azide results from experiments on two crystals are shown (Fig. 10). For one crystal the deformation stress increases from $13 \times 10^7 \text{ Pa}$ to $26 \times 10^7 \text{ Pa}$ as the load increases from about 10^{-1} N to $4 \times 10^{-1} \text{ N}$, whereas for the second crystal the deformation stress increases from $5 \times 10^7 \text{ Pa}$ to $10 \times 10^7 \text{ Pa}$ with the increase of load from $4 \times 10^{-2} \text{ N}$ to $2 \times 10^{-1} \text{ N}$. The results for three crystals of LAT type C and one of LAT type A are shown in Fig. 11. Crystal No. 1 shows an increase of deformation stress of over four times (i.e., from $\sim 5 \times 10^7 \text{ Pa}$ to $22 \times 10^7 \text{ Pa}$) as the load goes up from $2 \times 10^{-2} \text{ N}$ to $40 \times 10^{-2} \text{ N}$. However, in the other two crystals the variation of the deformation stress is not so marked; crystal No. 2 shows an increase of only 25% in the deformation stress, and from the small number of data points (four only) covering a relatively small load range (4 to $10 \times 10^{-2} \text{ N}$) for crystal No. 3, very little variation seems to occur.

In β -HMX crystals (Fig. 12) the variation of the deformation stress with load is from 25% (crystal No. 1) to a factor of 2 (crystal No. 2), though the load range of crystal No. 2 is considerably larger.

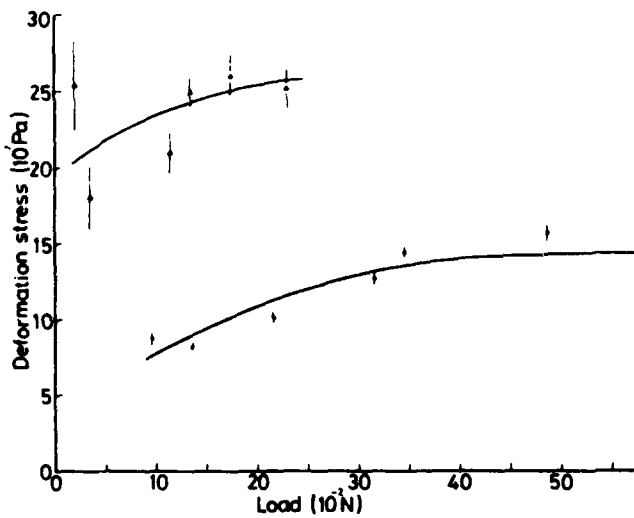


Figure 12 The variation of the deformation stress of β -HMX single crystals with load. Δ , crystal No. 1; \bullet , crystal No. 2.

One significant difference is the value of the stress at low loads; the deformation stress of one crystal is 3 to 4 times that of the other. In this case it does appear that the geometry of the contact is playing an important part; the lower stress values are for the slightly rounded crystal.

RDX crystals (Fig. 13) also show an increase in the value of the deformation stress by a factor of 2, as the load is increased from 2×10^{-2} N to 40×10^{-2} N. However, as for the other materials, there is a difference in the stress values of one crystal from that of the other.

For the KCl crystal (Fig. 14) the deformation stress remains constant at 2.7×10^7 Pa as the load increases from 4×10^{-2} N to 25×10^{-2} N.

It may be pointed out that for all the crystals studied, the size of the plastically deformed zone at the contact was not more than 1/50th of the size of the crystal. In other words, the plastic deformation was very localized.

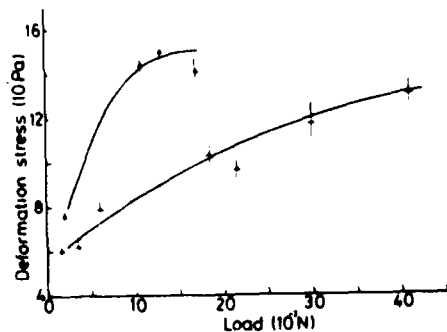


Figure 13 The variation of the deformation stress of RDX single crystals with load. \bullet , crystal No. 1; Δ , crystal No. 2.

5. Discussion

From the analysis of the data given in Section 4, several important observations can be made regarding the flow stresses of small (mm-size) single crystals of a number of brittle materials:

1. plastic flow occurs even for loads as small as 0.02 N;
2. generally, the flow stress increases with the applied load reaching a plateau at loads of 10^{-1} to 2×10^{-1} N;
3. the maximum deformation stress of a crystal is considerably smaller than its Vickers diamond hardness value (see Table II);
4. except for KCl, all crystals studied leave a film (composed of extremely small particles) on the glass surface against which they are compressed, even for loads as small as 10^{-2} N.

We shall discuss these observations separately.

5.1. Plastic flow at very low loads

The crystals used were as-grown and it is very likely

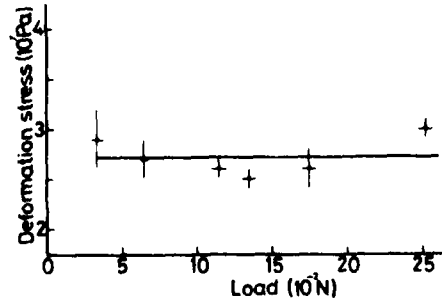


Figure 14 The variation of the deformation stress of a KCl single crystal with load.

that their mechanical behaviour would be that of non-work-hardened crystals. In fact, using the technique of indentation with a hard sphere, it has been found that the crystals of β -HMX and RDX show a considerable amount of work hardening. Now since some of the crystals possess "point-like" corners and some have "line-like" edges, the elastic limit will be exceeded at extremely low loads. This has been confirmed by the experimental observations reported in Section 3.

5.2. The increase of the deformation stress with load

The increase of the deformation stress with load is a little difficult to explain fully for conical, pyramidal and wedge-shaped crystals. It may be possible that a very limited number of slip systems available in these crystals is a contributory factor. It should be pointed out that in the case of cones and wedges of an isotropic material possessing more than five independent slip systems, such as in copper, the deformation stress is independent of the load for the fully work-hardened state and only increases by about 6% when the copper is annealed [14]. Therefore, for the brittle crystals studied, it is reasonable to assume that the work hardening effects will show some increase in the deformation stress with the increase of load. However, more experimental work is needed on other brittle crystals before almost a 100% increase in the deformation stress (see Figs. 10 to 13) with load can be understood.

For crystals whose loading edges were curved (e.g. RDX), the deformation stress against load behaviour is somewhat similar to that of an annealed metallic sphere; in both cases the stress initially increases with load, reaching a peak at higher loads. On comparison with the results from metallic spheres [15], it appears that the initial yield in the

crystal occurs at a value only just a few per cent higher than its uniaxial yield stress. The increase of the deformation stress with load can then be explained by the work hardening of the crystal.

5.3. The maximum deformation stress of a crystal against its Vickers diamond hardness

The maximum deformation stress and Vickers diamond hardness of the various crystals are compared in Table II. It is noted that in all cases the latter is considerably higher. Two factors responsible for the difference are:

- (i) the constraint imposed on a solid when a Vickers diamond pyramid is pushed into the solid is greater than when a corner or an edge of the solid is pressed against a hard flat surface; and
- (ii) the average plastic strain induced by the Vickers diamond pyramid indentation is 8%, whereas the strain induced due to the plastic deformation of a sharp-edged or pointed particle is dependent upon the included angle of the loaded zone, as has been shown for the case of annealed copper cones [14].

One important implication of these findings is that to predict the real area of contact of a brittle particle loaded against a hard flat surface using its Vickers diamond hardness value, as has been done by the previous investigators, is not generally correct; this approach gives very much an underestimate.

5.4. The layer left on the glass plate

Except for KCl, all crystals left a layer of microscopic particles on the glass plate even when compressed by as low a load as 1 g. There appear to be two possible explanations:

- (i) the crystals break up due to the compression; and

TABLE II Comparison of maximum deformation pressure of a particle and its Vickers diamond hardness

Material	Vickers diamond hardness* H_V (kg mm^{-2})	Maximum deformation pressure of particle P_m (kg mm^{-2})†	P_m/H_V
α -lead azide (PbN_4)	119.7 ± 8.1	27.5	0.23
RDX	24.1 ± 0.8	15	0.62
β -HMX	41.3 ± 1.0	26	0.63
LAT (type C)	109.4 ± 3.1	29	0.27
LAT (type A)	34.5 ± 0.9	12	0.35
KCl	16 ± 1	2.8	0.18

* Load on indentor was 15 g.

† Error $\approx 5\%$.

TABLE III Predicted minimum loads for compression cracking

Materials (all single crystals)	Predicted minimum* load for cracking (N)
α -lead azide	6.6×10^{-6}
RDX	1.2×10^{-3}
KCl	1.9×10^{-2}

*Calculated using H_V values.

(ii) the break up does not occur during the compression, but the adhesion between the crystal and the glass surface is so high that when the crystal is separated from the glass, fracture occurs within the crystal.

According to Hagan [16], the critical load P_α to cause cracking of a brittle particle by compression is given by:

$$P_\alpha \approx 880(K_{IC}/H_V)^3 K_{IC} \quad (3)$$

where K_{IC} is the critical stress intensity factor of the particle and H_V its Vickers diamond pyramid hardness. For plane strain conditions, $K_{IC} = [(2\gamma E)/(1 - \nu^2)]^{1/2}$ where γ is the fracture surface energy, E the Young's modulus, and ν the Poisson's ratio. The critical calculated loads to cause cracking are shown in Table III.

It will be seen from Table III that the crystals of PbN_6 , RDX and KCl should crack at the loads used in these experiments. It was pointed out above that the deformation pressures of the various crystals are considerably smaller than their Vickers hardness values (Table II). Therefore, if we use the maximum deformation pressures in Equation 3 in place of H_V , the predicted loads will be markedly higher, though both lead azide and RDX will still crack, but not KCl, for the loads employed here.

It must be pointed out that *in situ* observations of the explosive crystals did not show any cracking, suggesting that the adhered layer on the glass probably forms during the unloading (i.e. separation). However, irrespective of the fact whether cracking occurs during loading or unloading, the measurement of the area of real contact will not be affected.

The fact that when a particle of an explosive material comes into contact with a solid surface (e.g. a container), it leaves a thin layer of the explosive on the solid, means that the situation can be hazardous. Therefore, it is important to clean the surface of the container thoroughly after it has been in contact with an explosive, especially if it is of a primary type.

5.5. Flow stress determination

From the deformation stress values of a brittle particle, an estimate of its flow stress (i.e. yield stress at the imposed strain) can be made. If the particle is spherical, then the deformation stress at low loads will correspond closely to the uniaxial yield stress of the explosive crystals used in this work. The values are:

$$\begin{aligned} \alpha\text{-PbN}_6 &\leq 5 \times 10^7 \text{ Pa;} \\ \text{LAT type C} &\leq 5 \times 10^7 \text{ Pa;} \\ \text{LAT type A} &\leq 6.5 \times 10^7 \text{ Pa;} \\ \beta\text{-HMX} &\leq 7.5 \times 10^7 \text{ Pa;} \\ \text{RDX} &\leq 4 \times 10^7 \text{ Pa.} \end{aligned}$$

6. Conclusions

The plastic deformation stress of as-grown single crystals of a number of explosive materials has been successfully determined using a new experimental technique. The experiments involved measuring the real area of contact between the test crystal and a transparent glass plate pressed together with a given normal load. The deformation stress was found to increase with load, reaching a plateau at higher loads. It was discussed whether the plastic deformation stress of a particle approaches its uniaxial yield stress at low normal loads; estimates of the limiting values of the uniaxial yield stress of the explosive crystals have been given.

Acknowledgements

The author should like to thank Drs J. T. Hagan and E. H. Yoffe for comments on the manuscript, Dr P. H. Collins (PERME) for supplying the LAT crystals, and Dr J. E. Field and Mr S. J. P. Palmer for discussions on β -HMX crystals. The work was supported in part by the Ministry of Defence (Procurement Executive) and in part by the US Government through its European Research Office.

References

1. M. M. CHAUDHRI, *Nature* **263** (1976) 121.
2. D. TABOR, *J. Lub. Technol.* **103** (1981) 169.
3. J. T. HAGAN and M. M. CHAUDHRI, *J. Mater. Sci.* **12** (1977) 1055.
4. S. J. P. PALMER and J. E. FIELD, *Proc. Roy. Soc. A383* (1982) 399.
5. M. M. CHAUDHRI, PhD Thesis, University of Cambridge (1969).
6. C. S. CHOI and H. P. BOUTIN, *Acta Crystallogr. B25* (1969) 982.

7. MELANIE A. PIERCE-BUTLER, *ibid.* B38 (1982) 2681.
8. H. H.CADY, A. C. LARSON and D. T. CROMER, *ibid.* 16 (1963) 617.
9. C. S. CHOI and E. PRINCE, *ibid.* B28 (1972) 2857.
10. P. J. HALFPENNY, K. J. ROBERTS and J. N. SHERWOOD, *J. Mater. Sci.* 19 (1984) 1629.
11. H. D. MEGAW, "Crystal structures: A Working Approach" (Saunders Company, London, 1973) p. 82.
12. M. T. SPRACKLING, "The Plastic Deformation of Simple Ionic Crystals" (Academic Press, London, 1976) p. 23.
13. F. P. BOWDEN and D. TABOR, "The Friction and Lubrication of Solids" (Clarendon Press, Oxford, 1950) p. 5.
14. M. M. CHAUDHRI, *Phil. Mag.* A48 (1983) L15.
15. M. M. CHAUDHRI, I. M. HUTCHINGS and P. L. MAKIN, *ibid.* A49 (1984) 493.
16. J. T. HAGAN, *J. Mater. Sci. Lett.* 16 (1981) 2909.

*Received 24 November
and accepted 29 November 1983*

END

FILMED

7-85

DTIC